ROYAL SOCIETY
OF CHEMISTRY

PAPER

Check for updates

Electrochemical sensors based on the composite of reduced graphene oxide and a multiwalled carbon nanotube-modified glassy carbon electrode for simultaneous detection of hydroquinone, dopamine, and uric acid†

Wulan Tri Wahyuni, [iD] [ab] Shafa Aini Hasnawati Ta'alia,[a] Ari Yustisia Akbar, [iD] [c] Bunga Rani Elvira, [iD] [c] Irkham, [iD] [d] Isnaini Rahmawati, [iD] [e] Ruri Agung Wahyuono[f] and Budi Riza Putra [iD] *[c]

Using a simple drop-casting technique, we successfully fabricated a sensitive electrochemical sensor based on the composite of reduced graphene oxide (RGO) and multiwalled carbon nanotubes (MWCNT) deposited on the surface of a glassy carbon electrode (GCE) for individual and simultaneous measurements of hydroquinone (HQ), dopamine (DA), and uric acid (UA). The nanocomposite of RGO/MWCNT was further characterized in terms of its structural properties, surface morphology, and topography using Raman, FT-IR spectroscopy, SEM, HRTEM, and AFM. Then, the proposed sensor for simultaneous measurement of HQ, DA, and UA based on RGO/MWCNT-modified GCE was investigated for its electrochemical behavior and electroanalytical performances using cyclic voltammetry (CV) and electrochemical impedance spectroscopy (EIS), and differential pulse voltammetry (DPV). In addition, the composition ratio between RGO and MWCT was 1 : 1 showing the highest electrochemical response for simultaneous detection of HQ, DA, and UA. Owing to the synergistic effect between RGO and MWCNT leading to excellent conductivity properties, the proposed sensor exhibited improved electrochemical response at pH 7 toward the oxidation processes of HQ, DA, and UA on the surface of modified electrode. The proposed sensor demonstrated three well-defined anodic peaks of these analytes with their linear concentrations ranges of 3.0–150.0 μM for HQ, 4.0–100.0 μM for DA, and 2.0–70.0 μM for UA. The limit of detection values for the simultaneous detection of HQ, DA, and UA were found as follows 0.400 ± 0.014, 0.500 ± 0.006, and 0.300 ± 0.016 μM, respectively. The additional features of this proposed sensor are high reproducibility and stability for the simultaneous detection of HQ, DA, and UA with negligible interference effect from interferents such as Mg^{2+}, K^+, Cl^-, ascorbic acid, and glucose. An acceptable percentage of recovery was also shown by this sensor for simultaneous measurements of HQ, DA, and UA using 6 samples of human urine. In summary, the RGO/MWCNT nanocomposite has been shown to be a promising platform for rapid, simple, and reliable determination of simultaneous measurements of HQ, DA, and UA in practical applications.

1 Introduction

Electrochemical sensors have shown great promise for the simultaneous detection of multiple analytes in various fields including environmental markers and biological molecules due to their simplicity, rapid, sensitive, and efficient properties.[1,2] One of the attractive topics is the development of electrochemical sensors for the detection of several important

[a]*Analytical Chemistry Division, Department of Chemistry, Faculty of Mathematics and Natural Sciences, Kampus IPB Dramaga, Bogor 16680, Indonesia. E-mail: wulantriws@apps.ipb.ac.id*

[b]*Tropical Biopharmaca Research Center, IPB University, Bogor 16680, Indonesia*

[c]*Research Center for Metallurgy, National Research and Innovation Agency (BRIN), PUSPIPTEK Gd. 470, South Tangerang, Banten, 15315, Indonesia. E-mail: budi.riza.putra@brin.go.id*

[d]*Department of Chemistry, Faculty of Mathematics and Natural Sciences, University of Padjajaran, Bandung 45363, Indonesia*

[e]*Department of Chemistry, Faculty of Mathematics and Natural Sciences, University of Indonesia, Depok 16424, Indonesia*

[f]*Department of Engineering Physics, Faculty of Industrial Technology and Systems Engineering, Institut Teknologi Sepuluh Nopember, Jl. Arif Rahman Hakim, Kampus ITS Keputih-Sukolilo, Surabaya 60111, Indonesia*

† Electronic supplementary information (ESI) available. See DOI: https://doi.org/10.1039/d4ra05537c

biological molecules such as hydroquinone (HQ), dopamine (DA), and uric acid (UA) for further analytical applications. These three molecules have been employed in several recent studies of electrochemical sensors with substantial environmental and biological implications for the health of human beings.[3–6] HQ or 1,4-dihydroxybenzene is a common constituent of industrial effluents from coal tar production, oil refineries, leather, cosmetics, plastic, paper, steel, and pharmaceutical sectors.[7,8] This chemical has been recognized by the European Union (EU) and the United States Environmental Protection Agency (US EPA) as an environmental pollutant that poses health risks at high levels in humans such as dermatitis, irritation, fatigue, liver and kidney disease, and cancer.[9,10] In addition, the usage of HQ as skin-lightening cosmetics has been prohibited in many countries worldwide with a 2% permissible limit for topical treatments intended for dermatological purposes.[11] According to the Occupational Safety and Health Administration (OSHA) and Threshold Limit Values (TLV), the Permissible Exposure Limit (PEL) of hydroquinone to the human body is 2 mg m^{-3}.[12] Another previous work has reported that the HQ level in human urine in the concentration range of 0.6 to 4.2 μg mL^{-1} equivalent to 5.45–38.2 μM.[13]

Meanwhile, DA and UA are important biomolecules in regulating physiological processes in the human metabolism, central nervous, and renal system.[14,15] DA is an essential neurotransmitter that plays a significant role in neurological functions and its abnormal concentrations in the human body may be responsible for diseases such as Parkinson's disease and schizophrenia.[16] Several studies have found that the physiological concentrations of dopamine in the human body vary significantly within the urine and cerebral fluid at 5 nM and in blood at less than 0.13 nM.[17,18] Human blood also contains UA, a metabolic by-product of purine metabolism, which presents in normal levels at 140–420 μM, and its accumulation causes the blood to become more acidic which can lead to serious diseases such as hyperuricemia, gout, and Lesch-Nyhan syndrome.[19,20] Therefore, it is crucial to develop a simple and sensitive analytical method for the simultaneous detection of HQ, DA, and UA in synthetic solutions and real samples. This developed approach will be valuable for early detection of abnormal concentrations of these biological molecules and as a sign of potential disorders for human health.

Several analytical techniques based on high-performance liquid chromatography,[21–23] Raman spectroscopy,[24–26] fluorescence,[27,28] capillary electrophoresis,[29–31] gas chromatography-mass spectrometry,[32–35] chemiluminescence,[36–38] photoelectrochemical,[39–41] have been developed for the quantitative analysis of HQ, DA, and UA. These techniques have been widely applied as quality control procedures in many laboratories due to their sensitivity and accuracy in detecting these three biomolecules. Although the above methods have been developed in great advance based on their performances, there are still limitations to be addressed, including high cost, the need for sophisticated instruments, and time-consuming sample pretreatment. Compared to these methods, electrochemical methods have been widely developed for their benefits of simple, low cost, high sensitivity, rapid selectivity, portable, and

selectivity in detecting HQ, DA, and UA.[42–46] Furthermore, a thorough understanding of the electron transport kinetics of HQ, DA, and UA at the electrode surface is necessary to provide insight into chemical reactions in the biological system of human metabolism.

The morphology of reduced graphene oxide (RGO) as two-dimensional (2D) nanomaterials could provide a large surface area and high conductivity properties which is beneficial to be employed for sensor fabrication.[47,48] However, the enhanced conductivity of RGO might be lowered due to the possibility of restacking and aggregation by the presence of oxygen-containing groups on their 2D structures.[49,50] One way to improve the RGO conductivity is by incorporating it with multi-walled carbon nanotubes (MWCNT) to produce a stable dispersion of RGO and MWCNT nanocomposite *via* non-covalent interactions. This nanocomposite has demonstrated good electrical conductivity and high chemical and thermal stability which are advantageous to be employed as a material platform of electrochemical sensors.[51,52] The anticipated outcome of the unique properties of RGO and MWCNT could work synergistically to improve the electrochemical oxidation current of HQ, DA, and UA on the electrode surface. In addition, the nanocomposite of RGO and MWCNT has been previously employed as an electrode modifier for the simultaneous detection of nitrite and nitrate,[53] ascorbic acid, dopamine, and uric acid,[54,55] HQ, catechol, and resorcinol,[56,57] hydrogen peroxide, chlorine, and coenzyme,[58,59] bisphenol A, 8-hydroxy-2′-deoxyguanosine, and HQ,[60] and food dyes (Sunset Yellow and Tartrazine).[61]

To the author's knowledge, no published studies have reported on the simultaneous measurements of HQ, DA, and UA using nanocomposite consisting of RGO and MWCNT as a material platform of electrode modifiers for the electrochemical sensors. This proposed sensor is developed by modifying the surface of a glassy carbon electrode (GCE) with the RGO/MWCNT composite and employed for the simultaneous determination of HQ, DA, and UA in human urine samples. Based on the results of this work, RGO/MWCNT nanocomposite could improve the conductivity of the modified electrode and thus provide excellent electroanalytical performance for simultaneous detection of HQ, DA, and UA. Under optimum conditions, the proposed sensor shows a remarkable electrochemical response for simultaneous HQ, DA, and UA measurements with low detection limits. This proposed sensor exhibits good reproducibility and repeatability, and negligible effect from common species as potential interferences. In addition, an acceptable recovery percentage is obtained in the practical applications of this proposed sensor for the simultaneous determination of HQ, DA, and UA in 6 samples of human urine.

2 Experimental

2.1. Reagent and apparatus

Graphite powder with carbon content ≥99.95%, multiwalled carbon nanotubes (MWCNT) (>90% carbon basis with diameter *versus* length: 110–170 nm *versus* 5–9 μm), *N,N*-dimethylformamide (DMF) (≥99.8%) (CAS number: 68-12-2), KMnO$_4$

(≥99%), H_2SO_4 (95–98%), H_2O_2 30%, NaH_2PO_4 (≥99%), Na_2HPO_4 (≥99%), $NaNO_3$ (≥99%), $K_3[Fe(CN)_6]$ (≥99%), glucose (≥99%), urea (≥99%), ascorbic acid (≥99%), $MgSO_4$ (≥99%), uric acid (≥99%) (CAS number: 1198-77-2), dopamine hydrochloride (≥99%) (CAS number: 62-31-7), and hydroquinone (≥99%) (CAS number: 123-31-9) were obtained from Sigma Aldrich. All chemicals were of analytical grade and employed as received without further purification. Deionized water (conductivity ≈ 0.05 μS cm^{-1}) was used throughout the experiments.

The Raman spectra of graphite, graphene oxide (GO), and reduced graphene oxide (RGO) were derived from a Micro Confocal Hyperspectral 3D Imaging Raman Spectrometer (HORIBA LabRAM HR Evolution, Japan). Meanwhile, the infrared (IR) spectra from these materials using a Fourier transform infrared (FTIR) spectrometer (Infrared Bruker Tensor 37, Germany). The photograph of scanning electron microscopy (SEM) for RGO, multiwalled carbon nanotubes (MWCNTs), and its composites were obtained using SEM JEOL JSM-IT 200. Moreover, transmission electron microscope (TEM) images of RGO, MWCNT, and RGO/MWCNT composite were derived from an FEI Tecnai G^2 20 S-Twin TEM. The electrochemical impedance spectroscopy (EIS) studies were performed using Sensit BT (PalmSens BV, Houten, The Netherlands). All electrochemical experiments were conducted using PalmSens Emstat3+ Blue (PalmSens BV, Houten, The Netherlands) equipped with 3-electrodes systems. It comprises a glassy carbon electrode (GCE with 3 mm in diameter) from IJ Cambria Scientific, Ag/AgCl as the reference electrode, and platinum wire as the auxiliary electrode. All electrochemical experiments were performed using standard laboratory apparatus such as Pyrex glassware, analytical balance, and micropipettes for solution preparation at ambient temperature.

2.2. Synthesis of reduced graphene oxide (RGO) from graphite precursor

First, graphene oxide (GO) material was synthesized from graphite precursor following the modified Hummer's method.[62] Briefly, 1.0 g of graphite was mixed with 0.5 g of $NaNO_3$ in 25 mL of concentrated H_2SO_4 and subsequently cooled at 0 °C for 1 hour in stirring conditions. Then, 3.0 g of $KMnO_4$ was slowly added to the mixture solution, and the temperature was kept below 20 °C in stirring condition for 1 hour. Next, 50 mL of deionized water was added to the mixture solution to produce an exothermic reaction at 90–95 °C. The obtained solution was stirred for 1 hour and subsequently left for 30 minutes. The reaction in the mixture solution was finally terminated by adding 50 mL of H_2O_2 30% in stirring conditions for 1 hour. The solution mixture was cooled at room temperature, washed with deionized water, and air-dried to obtain the GO powder.

The reduction of GO material was achieved by using ascorbic acid as a reducing agent. Approximately 400 mg of GO powder was diluted in 400 mL of deionized water and added with 4.0 g of ascorbic acid in stirring conditions for 30 minutes at 60 °C. The reduced GO material was centrifuged at 4000 rpm for 40 minutes to remove the supernatant to obtain the black paste.

Next, H_2O_2 30% was added to the black paste in stirring condition for 30 minutes at 60 °C to oxidize the remaining ascorbic acid. The black product containing RGO material was obtained by centrifugation at 4000 rpm with subsequent washing using ethanol and deionized water. The resulting powder was dried in the oven for 24 hours at 120 °C.

The powder of RGO was characterized using Raman and FTIR spectroscopy to observe the changes in functional groups in its chemical structure.

2.3. Fabrication of GCE-modified RGO/MWCNT in different compositions

The stock solution of RGO was prepared with deionized water as a solvent while MWCNT was dissolved in DMF to obtain each concentration as 1 mg mL^{-1}. The composite solution containing RGO and MWCNT was prepared in 3 different compositions at the weight ratio of 1:1, 3:7, and 7:3 to obtain a total concentration of 1 mg mL^{-1}. Each composite solution was then stirred for 30 min and followed by sonication for 30 min. Next, about 4.0 μL of each composite solution was drop-casted onto the surface of a glassy carbon electrode (GCE). The GCE modified each composite solution was then placed in the oven at 85 °C for 5 min to obtain a stable film of RGO/MWCNT. Fig. 1a illustrates the schematic diagram of the fabrication process of RGO/MWCNT composite and its deposition on the surface of GCE.

2.4. Investigation of the electrochemical behaviour of GCE-modified RGO/MWCNT in different compositions

The electrochemical behaviour of bare GCE and modified GCE (RGO-modified GCE, MWCNT-modified GCE, and three different weight ratios of (7:3, 3:7, and 1:1) of RGO/MWCNT-modified GCE) were evaluated in 50 μM hydroquinone (HQ), 30 μM dopamine (DA), and 10 μM uric acid (UA) in 0.1 M of pH 7 phosphate buffer. The phosphate buffer was prepared by mixing 0.1 M NaH_2PO_4 with 0.1 M Na_2HPO_4 in certain volume ratio, then its final pH was adjusted into pH 7. Electroanalytical measurements for all modified electrodes were performed using differential pulse voltammetry (DPV) at a potential window of −0.2 V to +0.6 V versus Ag/AgCl, at a scan rate of 25 mV s^{-1}, a potential step of 5 mV, a potential pulse of 50 mV, and a pulse time of 0.1 s. All electroanalytical measurements for simultaneous detection of HQ, DA, and UA using the modified electrodes were carried out in triplicate experiments.

2.5. Evaluation of the electroanalytical performance of RGO/MWCNT-modified GCE

The analytical performance of the RGO/MWCNT-modified GCE was investigated in several analytical parameters involving linearity, limit of detection (LOD), limit of quantification (LOQ), reproducibility, sensitivity, precision, and stability. The electroanalytical measurement was investigated using the DPV technique at a potential window of −0.2 V to +0.6 V versus Ag/AgCl, at a scan rate of 25 mV s^{-1}, a potential step of 5 mV, a potential pulse of 25 mV, and a pulse time of 0.01 s.
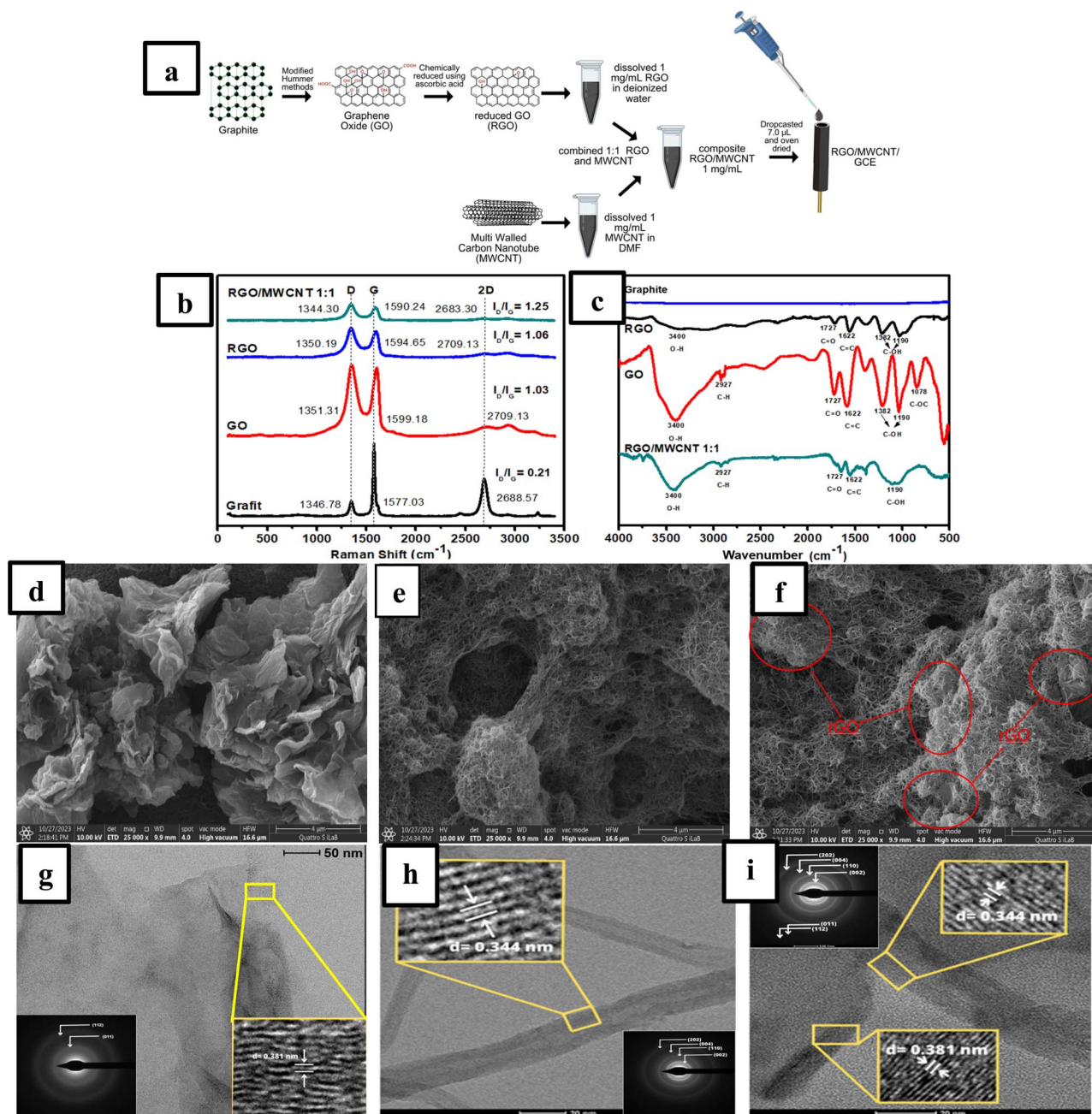
Fig. 1 (a) Schematic diagram of the fabrication process of the composite of reduced graphene oxide (RGO) and multiwalled carbon nanotubes (MWCNT) and its deposition onto the surface of glassy carbon electrode (GCE), (b) the Raman spectra and (c) infrared spectrum obtained from graphite, graphene oxide (GO), and reduced graphene oxide (RGO), the images of scanning electron microscope (SEM) in 25 000 times magnification derived from (d) RGO, (e) multiwalled carbon nanotube (MWCNT), and (f) the composite of RGO/MWCNT (1 : 1), high-resolution transmission electron microscopy (HRTEM) image and SAED pattern of (g) RGO, (h) MWCNT, and (i) RGO/MWCNT composite (1 : 1).

2.6. Linearity, LOD, and LOQ

The linearity of individual analytes by gradually decreasing the concentration of one compound while the concentrations of the other two compounds were fixed. LOD and LOQ were calculated based on the ratio of signal to noise (S/N $\approx$ 3 for LOD and S/N $\approx$ 10 for LOQ). Linearity was evaluated by measuring HQ solution in the concentration range of 3.0–53.0 μM with the concentrations of DA and UA being fixed at 4.0 μM and 2.0 μM in 0.1 M of pH 7 phosphate buffer. The linearity was also investigated by measuring DA solution in the concentration ranges of 4.0–34.0 μM with the concentrations of HQ and UA fixed at 3.0 μM and 2.0 μM in 0.1 M of pH 7 phosphate buffer. In addition, the linearity for UA was carried out by measuring the UA solution in the concentration range of 2.0–12.0 μM with the concentrations of HQ and DA being fixed at 3.0 μM and 4.0 μM in 0.1 M of pH 7 phosphate buffer. All measurements were performed in triplicate experiments using the DPV technique with the conditions

obtained from the previous experiment. Moreover, the HQ, DA, and UA measurements showed the maximum sensitivity when the coefficient of determination (R^2) close to 1 was obtained. The sensitivity value can be determined from the slope of the calibration curve which was calculated from triplicate experiments for simultaneous detection of HQ, DA, and UA.

2.7. Reproducibility, stability, and selectivity of the proposed sensor

The evaluation of sensor reproducibility was performed by preparing a solution containing 50.0 μM HQ, 30.0 μM DA, and 10.0 μM UA in 0.1 M of pH 7 phosphate buffer and measured with five individual electrodes of RGO/MWCNT (1 : 1)-modified GCE in triplicate experiments. Meanwhile, the sensor stability was evaluated by measuring the solution containing 50.0 μM HQ, 30.0 μM DA, and 10.0 μM UA in 0.1 M of pH 7 phosphate buffer in 7 repetitions using a similar electrode of RGO/MWCNT (1 : 1)-modified GCE. The sensor reproducibility and stability parameters were evaluated as a percentage of the relative standard deviation (%RSD) for simultaneous detection of HQ, DA, and UA. In addition, the selectivity of RGO/MWCNT (1 : 1)-modified GCE was investigated by simultaneously measuring HQ, DA, and UA in the presence of K^+, Mg^{2+}, and Cl^-, glucose, urea, and ascorbic acid as interfering compounds. Each interfering compound was prepared at a concentration of 50.0 μM and mixed with the solution containing 50.0 μM HQ, 30.0 μM DA, and 10.0 μM UA in 0.1 M of pH 7 phosphate buffer. The solution was then measured in triplicates using the DPV technique under similar previous experimental conditions.

2.8. Simultaneous detection of HQ, DA, and UA in the sample of human urine using RGO/MWCNT (1 : 1)-modified GCE

The performance of the RGO/MWCNT (1 : 1)-modified GCE for the simultaneous detection of HQ, DA, and UA was evaluated in the human urine samples using the DPV technique with the standard addition method. The human urine samples were obtained from 6 volunteers of healthy adults and diluted 100 times for simultaneous measurements of HQ, DA, and UA using 0.1 M of pH 7 phosphate buffer. Ethical consent for collecting human urine from adult healthy donors was received from IPB University, Indonesia. Informed written consent was obtained from all volunteers who contributed human urine to this work. The urine samples were collected in clean beakers under instruction to collect midstream urine from healthy volunteers. Samples were then collected and refrigerated within 4 hours of collection. Approximately, a 5 mL diluted sample of human urine was added with a standard solution in successive concentrations for HQ (5.0, 10.0, 15.0, 20.0, and 25.0 μM), for DA (3.0, 6.0, 9.0, 12.0, and 15.0 μM), and for UA (1.0, 2.0, 3.0, 4.0, and 5.0 μM). The human urine samples were then measured using the DPV technique with similar optimized experimental conditions in triplicates. The concentrations of HQ, DA, and UA in the sample of human urine were then calculated as the x-intercept of the standard addition calibration curve as follows in eqn (1):

$$x\text{-intercept} = -C_A \frac{V_o}{V_f} \tag{1}$$

where C_A is the concentration of HQ, DA, and UA in the human urine sample, V_o is the initial volume of the human urine, V_f is the final volume of the human urine sample, and x-intercept is derived when y is equivalent to zero.

3 Results and discussions

3.1. Materials characterization using Raman, IR spectroscopy, SEM, TEM, and AFM

Raman spectroscopy was employed to investigate the structural conversion from graphite into reduced graphene oxide (RGO) in the Raman shift between 50 to 3500 cm^{-1} as shown in Fig. 1b. Based on this figure, the Raman spectrum of graphite exhibits three prominent peaks at 1346.78, 1577.03, and 2688.57 cm^{-1}, respectively. The vibrations of carbon atoms with dangling bonds in plane termination of disordered graphite are linked to the peak at 1346.78 cm^{-1} (D-band, the breathing mode of k-point phonons of A_{1g} symmetry).[63] Meanwhile, the peak at 1577.03 cm^{-1} is associated with the vibration of sp^2-bonded carbon atoms and represents the E_{2g} mode of graphite.[64] In addition, the 2D band depends on the number of layers and stacking order in the graphite structure.[65] When graphite was oxidized to graphene oxide (GO), the D band became stronger at 1351.31 cm^{-1} implying a higher level of disorder of the graphene layers and defects during the chemical oxidation process.[66] In addition, the intensity ratio of the D band *versus* G band (I_D/I_G) from graphite (0.21) to GO (1.03) is significantly enhanced indicating the formation of sp^3 carbon through functionalization processes such as hydroxyl or epoxy causes the structural defects on its structure.[67] Furthermore, the intensity ratio of I_D/I_G is slightly increased after the reduction of GO due to the considerable shrinkage of the in-plane sp^2 domains leading to disordered structure in RGO materials.[68] Moreover, the highest intensity ratio of I_D/I_G was obtained in the RGO/MWCNT (1.25) showing an increase in the surface disorder of these nanocomposites. This enhancement might be attributed to the partial insertion of MWCNT into RGO layers which follows previous works on graphene-based nanocomposites.[69] FTIR was also performed for material characterization to confirm the changes in functional groups in each material.

Infrared (IR) spectroscopy was used to identify and characterize all materials by analyzing the frequency of functional groups related to the molecular or atomic vibrations. Fig. 1c shows the IR spectra obtained from 4 different materials (graphite, GO, RGO, and RGO/MWCNT composite) with no significant peak observed in graphite. Meanwhile, the presence of oxygen functional groups in GO has been revealed at 3400 cm^{-1} (O–H stretching vibrations), at 2927 cm^{-1} (C–H stretching vibrations), at 1727 cm^{-1} (C=O stretching vibrations), at 1600 cm^{-1} (C=C stretching vibrations), at 1382 and 1190 cm^{-1} (C–OH stretching vibrations), and 1078 cm^{-1} (C–OC stretching vibrations). The increase in IR spectrum obtained from GO might be due to the formation of several oxygen

functional groups in its structure such as alcohols, carboxylic acids, aldehydes, ketones, ethers, and epoxides.[70] In addition, when GO is reduced into RGO, the O–H stretching vibrations at 3400 cm^{-1} are significantly reduced due to the deoxygenation from the graphene structure. However, several stretching vibrations such as C=O at 1721 cm^{-1}, C=C at 1600 cm^{-1}, and C–OH at 1382 cm^{-1} become weaker due to the remaining carboxyl groups after the reduction of GO material. Furthermore, the IR spectra of RGO/MWCNT revealed the combination of previously mentioned absorption peaks from each RGO and MWCNT with less intensity than their parent materials. This is due to the co-existence of RGO in the MWCNT network resulting in the successful integration between these two materials. In addition, the IR spectra of this composite indicate the significant reduction of the oxygen as mentioned earlier functionalities upon the GO reduction.

Scanning electron microscope (SEM) analysis was employed to investigate the surface morphology of 3 electrode modifiers (RGO, MWCNT, and RGO/MWCNT composite) with magnifications of 25 000 times. Fig. 1d shows the SEM image of RGO which revealed thin sheets and randomly aggregated layers with distinct edges but crumpled on its surface. This rough surface is the common feature found in RGO materials obtained from the reduction of GO.[71] Meanwhile, Fig. 1e shows the characteristics of pristine MWCNT with a netlike structure which may offer a highly permeable region for the affinity adsorption of the analyte. In addition, this porous net structure of MWCNT provides an increased surface area which could offer an excellent ability for the electron transfer processes to the electrode surface. In addition, the incorporation of MWCNT into RGO

layers through noncovalent interactions between graphene sheets forms a three-dimensional (3D) network of RGO/MWCNT nanocomposite. As seen in Fig. 1f, the SEM image of this composite shows the unique structure in which the RGO material is coated with the fibrous network MWCNT leading to an enhancement of electrical conductivity. Thus, the synergistic properties in this nanocomposite are expected to be beneficial as a platform of electrochemical sensors for multicomponent simultaneous detection.

A transmission electron microscopy (TEM) study was employed to capture fine-detail images of RGO and MWCNT. Fig. 1g shows the high-resolution transmission electron microscopy (HR-TEM) image obtained from RGO revealing the sheet-like nature with less wrinkles and folding. In addition, the lattice fringes clearly shown in Fig. 1g confirm the interplanar distance for RGO material is 3.81 Å. Moreover, the crystallographic structure of RGO material was characterized by the selected area electron diffraction (SAED) method with the interplanar distance for RGO as 2.28 Å (011) and 1.21 Å (112) plane as shown in the inset of Fig. 1g. Meanwhile, the HR-TEM image of pristine MWCNT shows the regular tubular structure with a lattice fringe of 3.44 Å as shown in Fig. 1h. The selected area electron diffraction (SAED) of this nanomaterial also confirms several interplanar distances (inset Fig. 1h) with corresponding planes as 3.36 Å (002), 2.14 Å (110), 1.63 Å (004), and 1.23 Å (202) planes. Furthermore, the HR-TEM image of rGO/MWCNT nanocomposite (Fig. 1i) displays the lattice fringes for RGO and MWCNT with the corresponding interplanar distance of 3.81 and 3.44 Å, respectively. The SAED pattern of this nanocomposite (inset Fig. 1i) also reveals several number
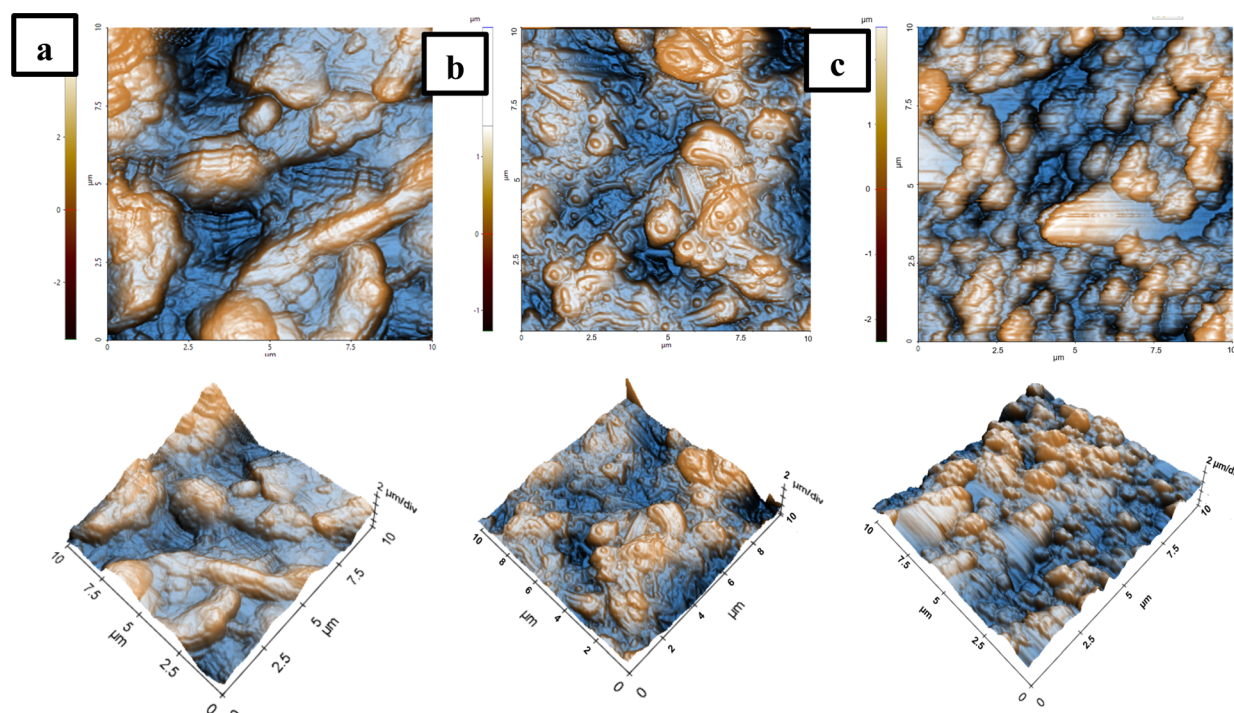

Fig. 2 AFM images in 2D (the first row) and 3D (the second row) dimension perspectives obtained from (a) reduced graphene oxide (RGO), (b) multiwalled carbon nanotubes (MWCNT), (c) composite of RGO and MWCNT (1 : 1).

interplanar distances for RGO as 0.87 (011) and 0.70 Å (112) planes and for MWCNT as 3.44 (002), 2.07 (110), 1.65 (004), and 1.21 (202) planes.

The atomic force microscopy (AFM) technique was employed to characterize the surface roughness and topography from three electrode materials (RGO, MWCNT, and RGO/MWCNT composite). Fig. 2 shows the AFM images of 2D (left section) and 3D (right section) obtained from these three different materials in a scan area of 10×10 μM with a scan rate of 0.5 Hz. From this investigation, it can be calculated three values of root-mean-square roughness (R_q) for RGO, MWCNT, and RGO/MWCNT composite as follows 37, 39.6, and 70.1 μm, respectively. In addition, the value of peak-to-valley (R_{pv}) was also derived from RGO, MWCNT, and RGO/MWCNT composite as 86.4, 73.8, and 184.4 μm, respectively. Both increases (R_q and R_{pv}) from the starting material (RGO and MWCNT) to its composite could be attributed to the strong noncovalent interaction that allows the good dispersion of MWCNT into RGO structures.[72] Moreover, the presence of MWCNT could prevent the restacking of graphene layers and act as a spacer in the interlayer spacing of RGO sheets thus increasing the surface area of its composite.[73,74] This high surface area of the RGO/MWCNT composite is advantageous to improve its conductivity and adsorption performance since it allows for more surface contact on the surface of modified electrode. Thus, it will be interesting to investigate the employment of this material composite as a platform for the development of electrochemical sensors for the simultaneous detection of electroactive biological molecules particularly for hydroquinone (HQ), dopamine (DA), and uric acid (UA) detection.

3.2. Studies of the charge-transfer behaviour of the modified electrodes

As the initial step to investigate the charge-transfer behaviour of the modified electrodes, cyclic voltammetry (CV) and electrochemical impedance spectroscopy (EIS) techniques were employed on 6 different electrodes (bare GCE, RGO/GCE, MWCNT/GCE, RGO/MWCNT (7 : 3)/GCE, RGO/MWCNT (3 : 7)/GCE, and RGO/MWCNT (1 : 1)/GCE). This study was conducted to determine the electrode conductivity of each modified electrode by measuring it using 1.0 mM $K_3[Fe(CN)_6]$ in 0.1 M KCl solution. Fig. 3a shows the cyclic voltammogram at a scan rate of 50 mV s^{-1} obtained from 6 different electrodes with the highest sensitivity observed at RGO/MWCNT (1 : 1)/GCE for both anodic and cathodic peak currents of Fe^{3+}/Fe^{2+} redox pair species compared to other electrodes. This result suggests that this electrode possesses the highest conductivity among other modified electrodes for the electron transfer electron process of Fe^{3+}/Fe^{3+} redox pair species. In addition, the magnitude of both anodic and cathodic peak currents of Fe^{3+}/Fe^{2+} redox pair species observed at all modified electrodes following the trend as follows: RGO/MWCNT (1 : 1)/GCE > RGO/MWCNT (3 : 7) > RGO/MWCNT (7 : 3) > MWCNT/GCE > RGO/GCE > bare GCE.

To further justify the result from CV studies, all modified electrodes were subjected to EIS studies to characterize the fundamental properties such as the phenomena of charge
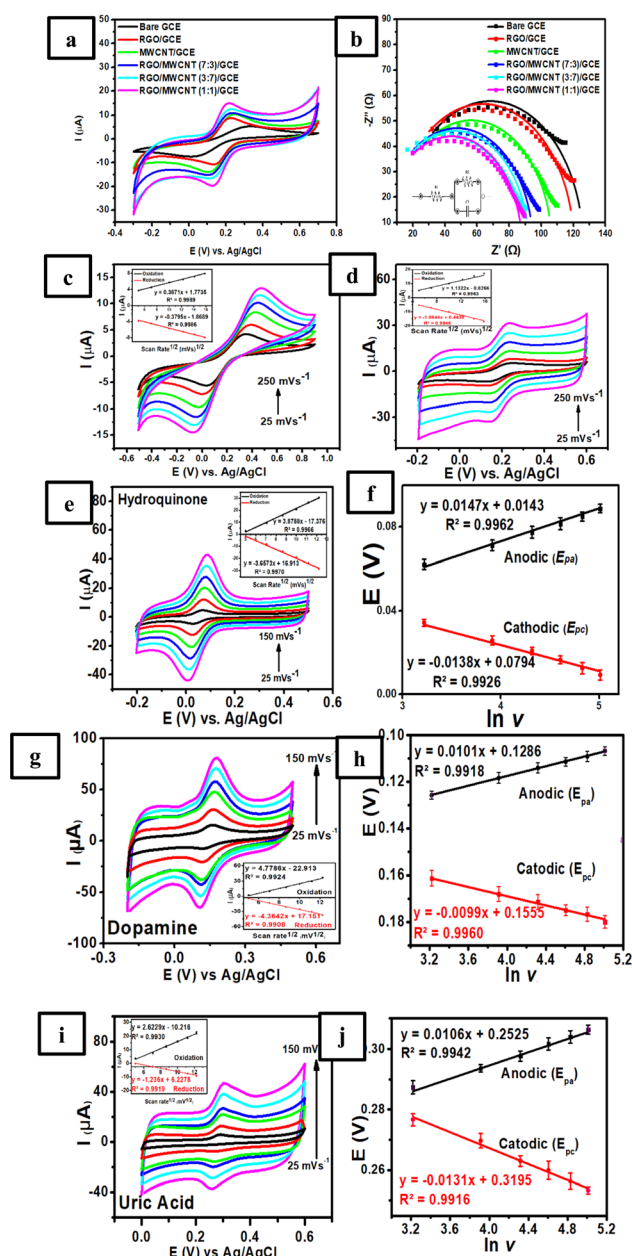

Fig. 3 (a) Voltammograms and (b) Nyquist plot derived from six different modified electrodes (bare GCE, RGO/GCE, MWCNT/GCE, 7 : 3, 3 : 7, and 1 : 1 RGO/MWCNT/GCE) for the measurements of 1.0 mM $K_3[Fe(CN)_6]$ in 0.1 M KCl solution at the frequency range from 1×10^5 Hz to 2×10^2 Hz and $E_{ac} = 6$ mV at an open-circuit potential. Voltammogram of 1 mM $K_3[Fe(CN)_6]$ in 0.1 M KCl measured with (c) bare GCE and (d) RGO/MWCNT (1 : 1)-modified GCE, voltammograms obtained from RGO/MWCNT (1 : 1)-modified GCE for the measurement of (e) 50 μM HQ, (g) 100 μM DA, and (i) 200 μM UA in 0.1 M of pH 7 phosphate buffer at various scan rates (25, 50, 75, 100, 125, and 150 mV s^{-1}). The linear relationship between the natural logarithm of the scan rates (ln v) and peak potential of anodic (E_{pa}) and cathodic (E_{pc}) for (f) HQ, (h) DA, and (j) UA measured with RGO/MWCNT (1 : 1)-modified GCE.

transfer resistance at the interface of electrode/electrolyte. The result from EIS studies of each modified electrode will correspond to the electrode conductivity as depicted by the Nyquist

plot from 6 different electrodes (Fig. 3b). Based on this figure, the Nyquist plot of each electrode was obtained by measuring 1.0 mM $K_3[Fe(CN)_6]$ in 0.1 M KCl solution in the frequency range from 10^5 Hz to 2×10^2 Hz with $E_{dc} = 0$ V and $E_{ac} = 6 \times 10^{-3}$ V at an open-circuit potential. Based on this figure, the semicircle (Nyquist plot) in the high-frequency region obtained from all electrodes can be attributed to the phenomena of the charge transfer resistance at the interface of electrode/electrolyte.[75] In addition, the diameter size of the Nyquist plot could be used to determine the charge transfer resistance (R_2) by fitting the experimental result with the corresponding Randles circuit as shown in the inset of Fig. 3b.

According to the calculations from EIS analysis, bare GCE showed the largest semicircle with the R_2 values of 118.5 Ω indicating the lowest conductivity among other modified electrodes. However, when the surface of GCE was modified with RGO and MWCNT, the R_2 value was decreased to 112.1 Ω for RGO/GCE and 100.6 Ω for MWCNT/GCE. In a further investigation, 3 different compositions of RGO and MWCNT were determined their R_2 values which resulted as 94.45 Ω for RGO/MWCNT (7 : 3)/GCE, 92.34 Ω for RGO/MWCNT (3 : 7)/GCE, and 88.2 Ω for RGO/MWCNT (1 : 1)/GCE. This result revealed that the combination of RGO and MWCNT in the composition ratio 1 : 1 showed the lowest resistance for the charge transfer process compared to other evaluated electrodes which agrees with several previous studies.[76,77] The heterostructure of a tube-like core of RGO/MWCNT composite, which fills in the gaps between the shell of graphene sheets and creates a continuously conductive network for electron transfer, is responsible for its high conductivity.[78] Therefore, RGO/MWCNT (1 : 1)-modified GCE was selected for further electrochemical investigations due to its highest electrical conductivity and showed considerable potential to be employed as electrode modifier materials.

3.3. The influences of scan rates on the modified electrodes

The effect of scan rate on bare GCE and RGO/MWCNT (1 : 1)-modified GCE was studied by measuring 1.0 mM $K_3[Fe(CN)_6]$ in 0.1 M KCl at various scan rates (25–250 mV s^{-1}). The current density can be used in this condition to calculate the geometric surface area of the working electrode as 7.06×10^{-2} cm^2. The studies of scan rate effect were performed using the CV technique for bare GCE for RGO/MWCNT (1 : 1)-modified GCE. Based on the inset Fig. 3c, bare GCE was found to be in a linear relationship of both currents of oxidation (I_{pa}) and reduction (I_{pc}) versus the square root of scan rates ($v^{1/2}$) with the corresponding calibration plot as I_{pa} (μA) = $0.3871v^{1/2}$ (mV s^{-1}) + 1.7735, $R^2 = 0.9989$ and I_{pc} (μA) = $-0.3795v^{1/2}$ (mV s^{-1}) − 1.8689, $R^2 = 0.9986$. This finding suggests that the electrochemical process on the surface of modified electrode was controlled by diffusion phenomenon. Meanwhile, RGO/MWCNT (1 : 1)-modified GCE also showed a linear relationship for both oxidation and reduction currents with the corresponding calibration plot as I_{pa} (μA) = $1.1322v^{1/2}$ (mV s^{-1}) − 0.8266, $R^2 = 0.9963$ and I_{pc} (μA) = $-1.0944v^{1/2}$ (mV s^{-1}) + 0.4638, $R^2 = 0.9946$ as shown in the Fig. 3d. Thus, it can be calculated the electrochemical active surface area (ECSA) for bare GCE and

RGO/MWCNT (1 : 1)-modified GCE based on the Randles–Sevcik equation as follows in eqn (2):

$$I_p = (2.69 \times 10^5)AD^{1/2}n^{3/2}v^{1/2}C \tag{2}$$

In this equation, I_p is the peak current (A), n is the number of transferred electrons during the electrochemical redox reaction of $K_3[Fe(CN)_6]$ ($n = 1$), A is the electrochemical active surface area of electrode (cm^2), D is the diffusion coefficient (6.70×10^{-6} cm^2 s^{-1}), C is the $K_3[Fe(CN)_6]$ concentration (mol cm^{-3}), and v is the scan rate (V s^{-1}). Based on this equation, the electrochemical active surface area (ECSA) for bare GCE and RGO/MWCNT (1 : 1)-modified GCE can be calculated as 2.88×10^{-2} and 4.96×10^{-2} cm^2, respectively. The ECSA of both modified electrodes is less than the geometric surface area (7.06×10^{-2} cm^2), perhaps due to surface heterogeneities caused by the RGO/MWCNT composite on the GCE surface. Thus, the ECSA of RGO/MWCNT (1 : 1)-modified GCE was approximately calculated as 2.2 times than obtained at bare GCE. The improved ECSA of RGO/MWCNT (1 : 1)-modified GCE compared to bare GCE is expected to enhance the electrocatalytic activity to be utilized as an electrochemical sensing platform for simultaneous detection of HQ, DA, and UA.

The relationship between scan rate and the electrochemical behaviors of 50.0 μM HQ, 100.0 μM DA, and 200.0 μM UA in 0.1 M of pH 7 phosphate buffer was also investigated to obtain the electron transfer mechanism at the electrode surface. The cyclic voltammograms obtained at different scan rates (25, 50, 75, 100, 125, and 150 mV s^{-1}) measured using RGO/MWCNT (1 : 1)-modified GCE are shown in Fig. 3e, g and i for HQ, DA, and UA, respectively. Based on these figures, the peak currents showed a linear relationship with the square root of the scan rate, suggesting the diffusion-controlled process predominates for HQ, DA, and UA on the electrode surface due to the fast electron transfer rate towards the RGO/MWCNT nanocomposite. As shown in the inset of Fig. 3e, g and i, the following linear relationship was observed: I_{pa} (μA) = $3.8788v^{1/2}$ (mV s^{-1}) − 17.376, $R^2 = 0.9966$ and I_{pc} (μA) = $-3.6573v^{1/2}$ (mV s^{-1}) + 16.913, $R^2 = 0.9970$ for HQ (inset Fig. 3e), I_{pa} (μA) = $4.7786v^{1/2}$ (mV s^{-1}) − 22.913, $R^2 = 0.9924$ and I_{pc} (μA) = $-4.3642v^{1/2}$ (mV s^{-1}) + 17.151, $R^2 = 0.9908$ for DA (inset Fig. 3g), and I_{pa} (μA) = $2.6229v^{1/2}$ (mV s^{-1}) − 10.216, $R^2 = 0.9930$ and I_{pc} (μA) = $-1.236v^{1/2}$ (mV s^{-1}) + 6.2278, $R^2 = 0.9919$ for UA (inset Fig. 3i). Thus, it can be concluded that all calibration plots showed good linearity with the electrochemical reaction of HQ, DA, and UA on the surface of RGO/MWCNT (1 : 1)-modified GCE was controlled by diffusion process.

In a further investigation of the scan rate effect on the peak potential of HQ, DA, and UA, it was revealed that the peak potential of oxidation (E_{pa}) shifted positively, and reduction (E_{pc}) shifted negatively with the increasing scan rate from 25 to 150 mV s^{-1}. The shifting of both potential peaks is linearly proportional to the natural logarithmic scan rate (ln v) for the reversible redox reactions observed in HQ, DA, and UA. The linear regression equations were $E_{pa} = 0.0147 \ln v + 0.0143$, $R^2 = 0.9962$ and $E_{pc} = -0.0138 \ln v + 0.0794$, $R^2 = 0.9926$ for HQ (Fig. 3f), $E_{pa} = 0.0161 \ln v + 0.1162$, $R^2 = 0.9915$ and $E_{pc} =$

$-0.0137 \ln v + 0.1825$, $R^2 = 0.9908$ for DA (Fig. 3h), and $E_{pa} = 0.0101 \ln v + 0.2652$, $R^2 = 0.9936$ and $E_{pc} = -0.012 \ln v + 0.9959$, $R^2 = 0.9926$ for UA (Fig. 3j). Based on Laviron's theory for the reversible process of electron transfer on the surface of modified electrode, the relationship between the peak potential of anodic (E_{pa}) and cathodic (E_{pc}) versus the scan rate (v) can be determined using the following eqn (3)–(6):

$$E_{pa} = E^{o} + \frac{RT}{\alpha nF} \ln v \qquad (3)$$

$$E_{pc} = E^{o} - \frac{RT}{(1-\alpha)nF} \ln v \qquad (4)$$

$$\log k_s = \alpha \log(1-\alpha) + (1-\alpha)\log\alpha - \log\frac{RT}{nFv} - \frac{\alpha(1-\alpha)nF\Delta E_p}{2.3RT} \qquad (5)$$

$$E_p = E^{\ominus} + \frac{RT}{\alpha nF} \ln\frac{RTK^{\ominus}}{\alpha nF} - \left(\frac{RT}{\alpha nF}\right)\ln v \qquad (6)$$

where n is the number of transferred electrons, α is the coefficient of electron transfer, F is the Faraday constant (96 485.33C mol^{-1}), R is the universal gas constant (8.314 J mol^{-1} K^{-1}), T is the absolute temperature constant (298 K), v is the scan rate, $E^{\ominus}$ is the formal potential, and $K^{\ominus}$ is the standard potential. It can be obtained from the above equations the values for n and α are $1.74 \approx 2$ and $0.79 \approx 1$ for HQ, $1.59 \approx 2$ and $0.79 \approx 1$ for DA, and $1.95 \approx 2$ and $1.27 \approx 1$ for UA. Thus, it can be deduced that the redox reactions of HQ, DA, and UA involved 2H$^+$ and 2e$^-$ at the electrode/electrolyte interface. Scheme 1 outlines the possible reaction mechanism of HQ, DA, and UA at the electrode surface.

Accordingly, based on Laviron's theory, the electron transfer rate constant (k_{et}) for HQ, DA, and UA can be calculated as follows 0.58, 0.80, and 4.5 s^{-1}, respectively which are still comparable to the values reported in the previous studies as 0.338 s^{-1} for HQ (as reported in ref. 79), 0.71 s^{-1} for DA (as reported in ref. 80), and 6.1 s^{-1} for UA (as reported in ref. 81). Moreover, the surface coverage of HQ, DA, and UA on the surface of RGO/MWCNT (1 : 1)-modified GCE can be calculated using the following eqn (7):

$$I_p = \frac{n^2F^2A\Gamma v}{4RT} \qquad (7)$$

where n, F, v, R, and T have similar meanings to the previous equation, A is the electrode area (cm^2), and Γ is the surface coverage (mmol cm^{-2}). Based on the slope of the plot of I_p versus v, the surface coverage of HQ, DA, and UA adsorbed on the surface of RGO/MWCNT (1 : 1)-modified GCE was calculated to be 3.15×10^{-5}, 1.71×10^{-5}, and 7.76×10^{-6} mmol cm^{-2}, which is comparable to those published previously.[82–84]

3.4. Chronoamperometric studies of HQ, DA, and UA in RGO/MWCNT (1 : 1)-modified GCE

The chronoamperometric studies were performed to study the performance of RGO/MWCNT (1 : 1)-modified GCE as a working electrode towards the electrocatalytic oxidation of HQ, DA, and UA in 0.1 M of pH 7 phosphate buffer. The potential of RGO/MWCNT (1 : 1)-modified GCE was fixed at 0.152 V vs. Ag/AgCl for HQ, 0.220 V vs. Ag/AgCl for DA, and 0.360 V vs. Ag/AgCl for UA. As shown in Fig. 4a–c, three chronoamperograms (plot of the current values versus $t^{-1/2}$) were obtained and the diffusion coefficient value can be calculated using the Cottrell eqn (8).

$$I = nFAD^{1/2}C\pi^{-1/2}t^{-1/2} \qquad (8)$$

where n, F, and A have similar meanings to the previous equation, D is the diffusion coefficient (cm^2 s^{-1}), and C is the concentration (mol cm^{-3}). Based on the inset Fig. 4a–c, the linear relationship between I versus $t^{-1/2}$ with calculated D
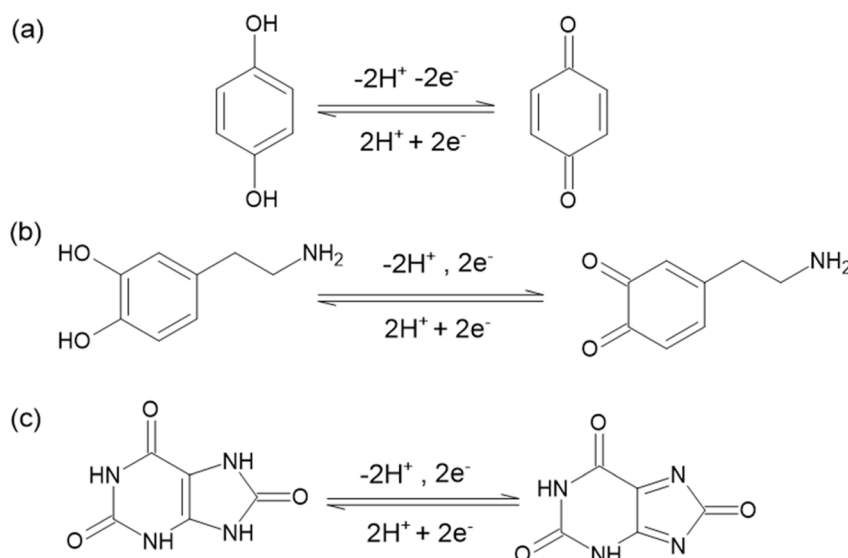
Scheme 1 The mechanisms of possible electrochemical reactions for (a) HQ, (b) DA, and (c) UA on the surface of RGO/MWCNT(1 : 1)-modified GCE.
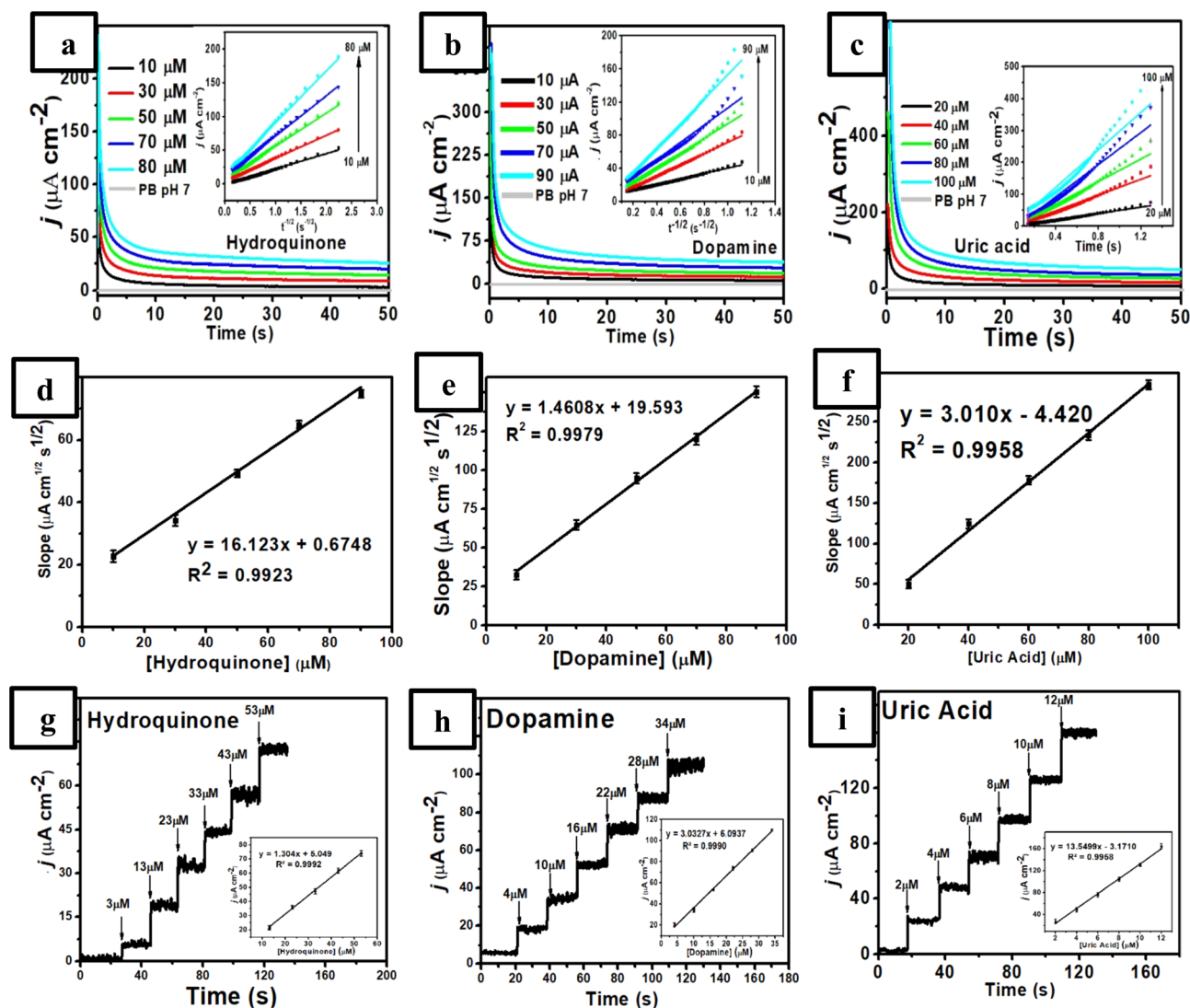
Fig. 4 Amperometric response of RGO/MWCNT (1 : 1)-modified GCE in 0.1 M of pH 7 phosphate buffer to different concentrations of (a) HQ (10.0–70.0 μM) at the applied potential of (E_{dc}) 0.152 V *vs.* Ag/AgCl, (b) DA (10.0–90.0 μM) at the applied potential of (E_{dc}) 0.220 V *vs.* Ag/AgCl, (c) UA (20–100 μM) at the applied potential of (E_{dc}) 0.360 V *vs.* Ag/AgCl. Calibration plot of the concentration of (d) HQ, (e) DA, and (f) UA *versus* the peak of their oxidation current. The amperogram obtained from the successive addition of (g) HQ in the concentration range of 3.0–53.0 μM in the presence of 4.0 μM DA and 2.0 μM UA, (h) DA in the concentration range of 4.0–34.0 μM in the presence of 3.0 μM HQ and 2.0 μM UA, and (i) UA in the concentration range of 2.0–12.0 μM in the presence of 3.0 μM HQ and 4.0 μM DA.

values for HQ, DA, and UA were 6.83×10^{-6}, 2.79×10^{-6}, and 9.97×10^{-6} cm^2 s^{-1}. These D values were following those previously reported studies as 8.9×10^{-6} cm^2 s^{-1} for HQ (in ref. 85), 2×10^{-6} cm^2 s^{-1} for DA (in ref. 86), and 2.75×10^{-6} cm^2 s^{-1} for UA (in ref. 87). In addition, Fig. 4d–f show the three calibration plots corresponding to the amperometric response of RGO/MWCNT (1 : 1)-modified GCE at different HQ, DA, and UA concentrations.

A quantitative analysis was also performed using the chronoamperometric studies by recording amperogram response from the measurements of HQ in the presence of DA and UA at 0.152 V *vs.* Ag/AgCl, DA in the presence of HQ and UA at 0.220 V *vs.* Ag/AgCl, and UA in the presence of HQ and DA at 0.360 V *vs.* Ag/AgCl. Fig. 4g–i display a good linearity corresponding to their

increasing concentrations with the successive additions of HQ (3.0–53.0 μM), DA (4.0–34.0 μM), and UA (2.0–12.0 μM) in various concentrations under stirring in 0.1 M of pH 7 phosphate buffer. In addition, from the inset Fig. 4g–i, it was obtained three equations of calibration curve for HQ at the concentration range of 3.0–53.0 μM with $I_p = 1.304x + 5.049$, $R^2 = 0.9992$, for DA at the concentration range of 4–34 μM with $I_p = 3.0327x + 6.0937$, $R^2 = 0.9990$, and for UA at the concentration range of 2–12 μM with $I_p = 13.5499x - 3.1710$, $R^2 = 0.9958$. Furthermore, the proposed sensor exhibits a rapid and stable current response toward HQ, DA, and UA oxidation with a response time of 0.4, 0.2, and 0.2 s, respectively (Fig. S1, ESI†). These results revealed that the independent measurements of three analytes (HQ, DA, and UA) are possible using the

chronoamperometric technique without any interference with an excellent linear relationship.

The influence of RGO/MWCNT composition in terms of its concentration in the weight/volume ratios on the intensity of anodic peak current of the modified electrode was also investigated using the DPV technique. Fig. 5b shows the current intensity reaches its maximum with each concentration of 1 : 1 in mg mL^{-1} unit of RGO/MWCNT when it was employed for the simultaneous measurement of 50 μM HQ, 30 μM DA, and 10 μM UA in 0.1 M of pH 7 phosphate buffer. Above the concentration of RGO/MWCNT (1 : 1) in mg mL^{-1} unit, there is a clear reduction in the peak current for HQ, DA, and UA, most likely caused by decreased conductivity on the electrode surface. This result indicates that a small proportion of RGO/MWCNT could give the highest conductivity of the modified electrode. Still, a higher concentration of this material composite lowered its electrocatalytic activity. This result might be due to a higher concentration of RGO/MWCNT composite, graphene as a two-dimensional material tends to stack together through non-covalent interactions which causes the blocking of catalytically active sites on the modified electrodes.[88] In addition, MWCNT might be aggregated at higher concentrations due to its van der Waals forces which produce an inhomogeneous dispersion composite and thus lowered the conductivity of nano-composite.[89] Therefore, 1 mg mL^{-1} concentrations for RGO and

MWCNT materials were employed for the subsequent experiments for simultaneous measurements of HQ, DA, and UA.

Fig. 5c shows the schematic illustration of a synergistic effect of the RGO/MWCNT composite on the GCE surface which is due to noncovalent interactions and van der Waals forces leading to the formation of an interconnected network structure between graphene layers and carbon nanotubes. This type of interaction could reduce the gap between RGO and MWCNT and facilitate a faster electron transport process on the electrode surface thus resulting in high electrical conductivity.[90] In addition, the non-covalent interaction between sp^2-hybridized regions of RGO with the sidewalls of MWCNT could promote the exfoliation of graphene layers and allow the entanglement of carbon nanotubes to expand resulting in a large surface area of RGO/MWCNT composite.[91] Moreover, the porous structure of RGO/MWCNT composite on the electrode surface is beneficial in reducing the overpotential and separating the oxidation potentials of HQ, DA, and UA from each other. MWCNT could significantly enhance the oxidation currents of HQ, DA, and UA by accelerating the electron transfer rate to the electrode surface due to its high electronic conductivity and large surface area. This could be useful for the discrimination of HQ, DA, and UA during its experimental investigation using voltammetric techniques. Thus, the synergistic effects of the electrocatalytic activity between RGO and MWCNT provided the RGO/MWCNT-
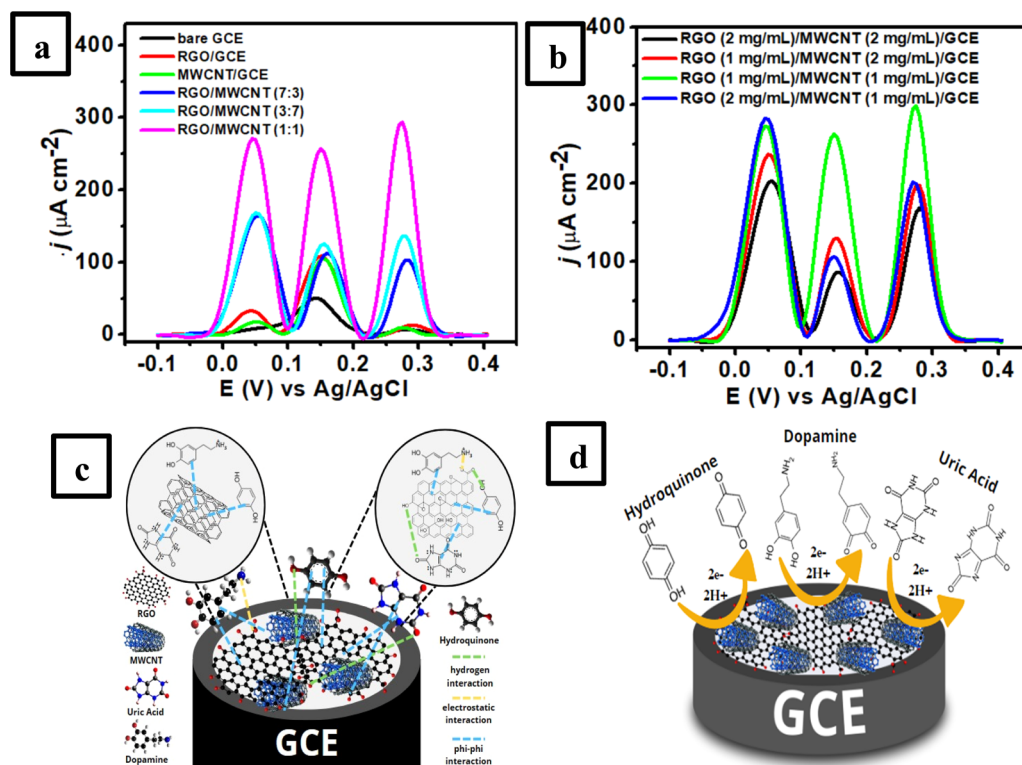

Fig. 5 Voltammograms at a scan rate of 25 mV s^{-1} were recorded from the simultaneous determination of 50 μM HQ, 30 μM DA, and 10 μM UA in 0.1 M of pH 7 phosphate buffer on (a) 6 different electrodes (bare GCE, RGO/GCE, MWCNT/GCE, RGO/MWCNT (7 : 3, 3 : 7, and 1 : 1)-modified GCE), (b) 4 different concentrations of RGO/MWCNT in % w/v (2 : 2, 1 : 2, 2 : 1, and 1 : 1), schematic illustration of (c) the chemical bonding occur in the composite of RGO/MWCNT and its interaction with HQ, DA, and UA on the surface of a GCE, (d) the oxidation mechanism of HQ, DA, and UA on the surface of RGO/MWCNT-modified GCE.

modified GCE with improved catalytic properties toward simultaneous detection of HQ, DA, and UA, which helped to distinguish these analytes. Fig. 5d displays the electrochemical oxidation mechanisms of HQ, DA, and UA on the surface of GCE modified with RGO/MWCNT composite to improve their anodic current responses.

As illustrated in Fig. 5c and d, the improvement in anodic current response could be attributed to the different interactions between three molecules with the composite of RGO/MWCNT-modified GCE. It is well known that RGO still bears negative charges due to a few oxygen-functional groups such as carboxyl, hydroxyl, and epoxy in its structure[92] which could assist the interaction with the target molecules (HQ, DA, and UA). For HQ, forming a noncovalent interaction between hydroquinone and graphene basal plane in RGO would enhance the anodic peak current. Meanwhile, DA shows the electrostatic interaction between positively charged DA and negatively charged RGO also the noncovalent interaction between DA and

the graphene layer is abundant with a hexagonal carbon structure. Nevertheless, the increased peak current of UA might be attributed to the formation of hydrogen bonds at the amide group in UA with an oxygen-rich functional group at the RGO-MWCNT composite.

3.5. Analytical performance of RGO/MWCNT (1 : 1)-modified GCE for simultaneous detection of HQ, DA, and UA

The electrooxidation of each analyte in the mixture solution was investigated by varying the concentration of a species with the other two concentrations remaining constant to further illustrate the feasibility of the proposed sensor for simultaneous detection of HQ, DA, and UA. It was revealed that the spiking of one target analyte showed a negligible effect on the peak currents and peak potentials of the other two analytes. Fig. 6a shows the DPV of RGO/MWCNT (1 : 1)-modified GCE at different concentrations of HQ (3–150 μM HQ) with a constant concentration of DA (4 μM) and UA (2 μM UA) in 0.1 M of pH 7

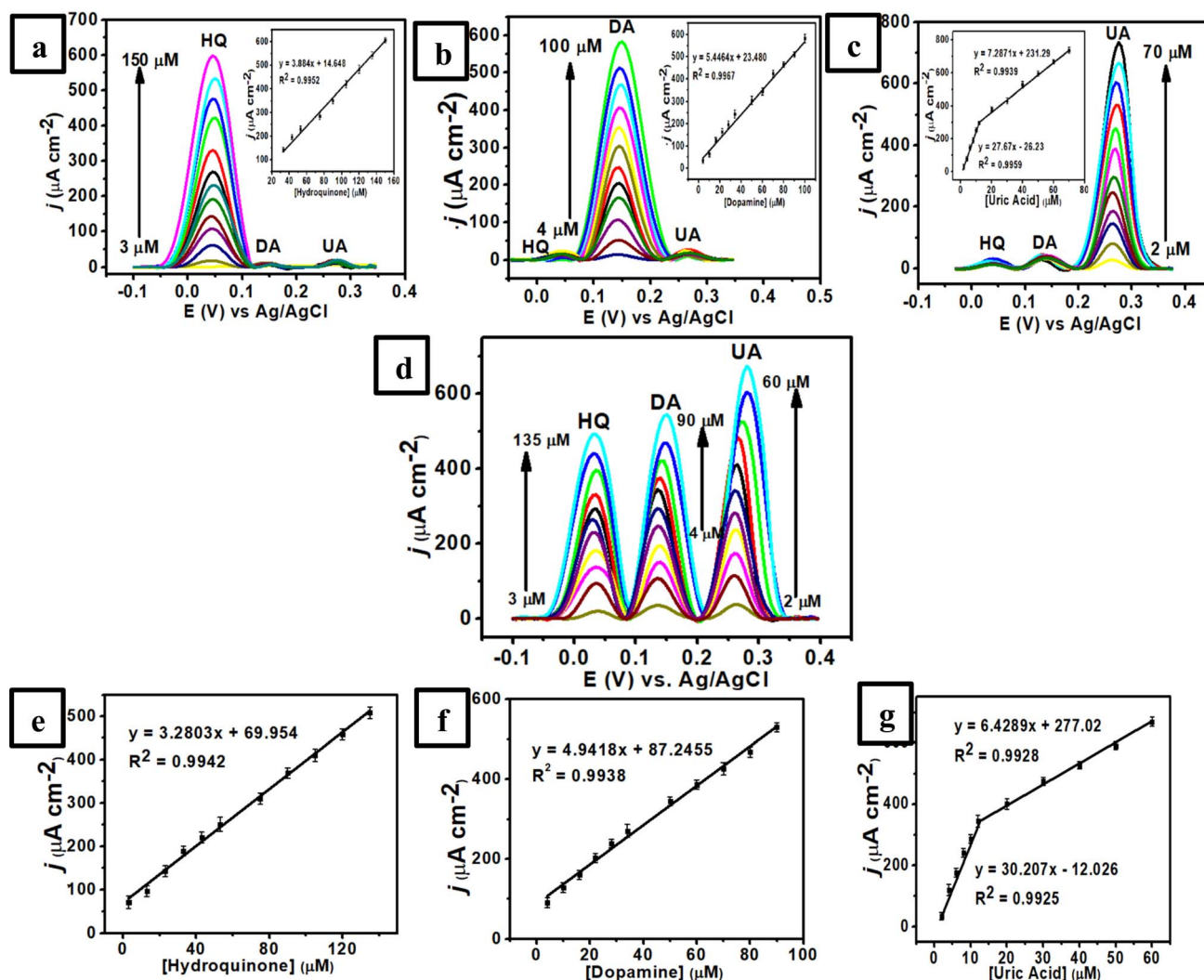**Fig. 6** Voltammogram obtained at a scan rate of 25 mV s⁻¹ from the simultaneous measurements of the mixture solution of 0.1 M of pH 7 phosphate buffer containing (a) 3–150 μM HQ, 4 μM DA, and 2 μM UA, (b) 3 μM HQ, 4–100 μM DA, and 2 μM UA, (c) 3 μM HQ, 4 μM DA, and 2–70 μM UA, (d) 3–153 μM HQ, 4–90 μM DA, and 2–60 μM UA using RGO/MWCNT (1 : 1)-modified GCE, the corresponding calibration plot obtained from the simultaneous measurement of various concentrations of (e) HQ, (f) DA, and (UA) versus their anodic peak currents.

phosphate buffer. As displayed in this figure, the obtained anodic peaks for these three species were separated under similar conditions to those of DPV studies with the peak current of HQ increased linearly from 3–150 μM at fixed concentrations of DA and UA. The inset in Fig. 6a also shows the linear equation for HQ as I_{pa} (μA) = 3.884$C_{hydroquinone}$ (μM) + 14.648 (R^2 = 0.9952, 3–53 μM with the sensitivity of 3.884 μA μM^{-1} cm^{-2}). Meanwhile, Fig. 6b displays the anodic current of DA enhanced linearly at various concentrations from 4–100 μM while the other concentrations of HQ and UA remained constant. The corresponding linear equation of DA is defined by I_{pa} (μA) = 5.4464$C_{dopamine}$ (μM) + 23.480 (R^2 = 0.9967, 4–100 μM with the sensitivity of 5.4464 μA μM^{-1} cm^{-2}) as displayed in the inset Fig. 6b. In addition, the peak current of UA increased linearly when its concentration changed from 2–12 μM (linear range 1) and 12–70 μM (linear range 2) at fixed concentrations of HQ and DA (Fig. 6c). The linear function of UA concentrations versus the peak current can be defined as I_{pa} (μA) = 27.67$C_{uric\ acid}$ (μM) − 26.23 (R^2 = 0.9959, 2–12 μM with the sensitivity of 27.57 μA μM^{-1} cm^{-2}) and I_{pa} (μA) = 7.2871$C_{uric\ acid}$ (μM) + 231.29 (R^2 = 0.9939, 12–70 μM, with the sensitivity of 7.2871 μA μM^{-1} cm^{-2}) (inset Fig. 6c).

In a subsequent experiment, the concentrations of HQ, DA, and UA were increased simultaneously to confirm the effect of each analyte in the presence of the other two species. Fig. 6d

shows three well-separated peaks of HQ, DA, and UA with their peak currents proportional to each concentration in a linear relationship. Then, it can be obtained the linear equations for HQ (Fig. 6e) as I_{pa} (μA) = 3.2803$C_{hydroquinone}$ (μM) + 69.954 (R^2 = 0.9942, 3–135 μM, with the sensitivity of 3.2803 μA μM^{-1} cm^{-2}), for DA (Fig. 6f) as I_{pa} (μA) = 4.9418$C_{dopamine}$ (μM) + 87.2455 (R^2 = 0.9937, 4–90 μM, with the sensitivity of 4.9418 μA μM^{-1} cm^{-2}), and for UA (Fig. 6g) as I_{pa} (μA) = 30.207$C_{uric\ acid}$ (μM) − 12.026 (R^2 = 0.9925, 2–12 μM) and I_{pa} (μA) = 6.4289$C_{uric\ acid}$ (μM) + 277.02 (R^2 = 0.9928, 12–60 μM) with the sensitivity of 6.429 μA μM^{-1} cm^{-2}. Thus, the limit of detection (LOD) (S/N ≈ 3) for HQ, DA, and UA can be determined as 0.400 ± 0.014, 0.500 ± 0.006, and 0.300 ± 0.016 μM, respectively. In addition, the limit of quantification (LOQ) (S/N ≈ 10) for HQ, DA, and UA were 0.800 ± 0.044, 1.000 ± 0.011, and 0.600 ± 0.025 μM, respectively. Furthermore, the performance of this sensor based on RGO/MWCNT (1 : 1)-modified GCE can be compared to those previously reported sensors which can be summarized in Table 1.

3.6. Reproducibility, stability, and selectivity of RGO/MWCNT (1 : 1)-modified GCE

The reproducibility of RGO/MWCNT (1 : 1)-modified GCE was investigated by measuring 50 μM UA, 30 μM DA, and 10 μM UA in 0.1 M of pH 7 phosphate buffer using five electrodes for each

Table 1 Comparison of the performance of RGO/MWCNT (1 : 1)-modified GCE with some reported works for determination of HQ, DA, and UA

Electrode	Analyte	Linear range (μM)	LOD (μM)	Sensitivity (μA μM^{-1} cm^{-2})	Ref.
PtNPs@CPOFs[a]-MWCNTs	HQ	6–500	0.66	0.082	3
Co-AcNC-3[b]/GCE	HQ	4–300	0.034	21.597	4
Bi$_2$WO$_6$/GCE	HQ	20–2500	4.1	1.5	93
Ce$_2$(WO$_4$)$_3$/CPE[c]	HQ	0.4–45	0.06	6.22 × 10^{-5}	94
AuNPs/LYH-47[d]/GCE	HQ	1–100	0.2	0.8	95
TT-COF(Co)/N-CNTs[e]/GCE	HQ	0.003–300	0.81 × 10^{-3}	0.094	96
Ni$_3$ZnC$_{0.7}$/Ni/GCE	HQ	0.3–100	0.14	0.735	97
N,Si-GQDs[f]	HQ	5–200	1.35	0.0097	98
Co,Mo@CNFs[g]/GCE	DA, UA	DA: 0.01–1000	DA: 0.00235	0.86	5
		UA: 1–1000	UA: 0.16	0.65	
h-WO$_3$/MoO$_3$/MoS$_2$/GCE	DA, UA	DA: 1.25–495	DA: 0.539	3.185	6
		UA: 10–1330	UA: 2.402	0.814	
Au@Cu-MOF/SPCE[h]	DA, UA	DA, UA: 10–1000	DA: 3.40	0.231	12
			UA: 10.36	0.275	
PANI[i]/Cu$_2$O-Au$_x$/GCE	DA, UA	DA: 0.01–200	DA: 0.0076	0.054	13
		UA: 0.1–1000	UA: 0.035	0.026	
Au@Ni-MOF	DA, UA	DA, UA: 0.5–1000	DA: 0.027	1.43	99
			UA: 0.028	1.35	
ZnO/CQDs[j]/CPE	DA, UA	DA: 0.12–142	DA: 0.46	3.375	100
		UA: 0.5–222	UA: 0.23	2.411	
Ti$_3$C$_2$T$_x$/TiO$_2$ NMs/GCE	DA, UA	DA: 2–33	DA: 0.093	0.133	101
		UA: 2–33	UA: 0.038	0.321	
ErGO/PEDOT:PSS (7 : 3)/GCE	DA, UA	DA: 10–110	DA: 0.5	0.6365	102
		UA: 3–33	UA: 0.4	0.1439	
RGO/MWCNT/GCE	HQ, DA, UA	HQ: 3–150	HQ: 0.4	3.280	This work
		DA: 4–100	DA: 0.5	4.942	
		UA: 2–70	UA: 0.3	6.429	

[a] Covalent polyoxometalate–organic frameworks. [b] Co-based single atom nanozymes anchored on HOH-activated ZIF-derived porous carbon. [c] Carbon paste electrode. [d] Layered yttrium hydroxide. [e] Co-porphyrin-based covalent organic framework. [f] Graphene quantum dots. [g] Electrospun nanofibers. [h] Screen-printed carbon electrode. [i] Polyaniline. [j] Carbon quantum dots.

analyte. The reproducibility experiments were performed using five individual modified electrode in triplicate experiments utilizing the DPV technique at a scan rate of 25 mV s^{-1} and a potential range from −0.2 to 0.6 V *vs.* AgCl. Fig. 7a shows the values of relative standard deviation (% RSD) obtained from this work for HQ, DA, and UA were 1.53, 2.14, and 2.59%, respectively. This result demonstrated a satisfactory reproducibility of RGO/MWCNT (1 : 1)-modified GCE for simultaneous detection of HQ, DA, and UA. Meanwhile, the stability of RGO/MWCNT (1 : 1)-modified GCE was also evaluated by measuring a solution containing 50 μM UA, 30 μM DA, and 10 μM UA in 0.1 M of pH 7 phosphate buffer in 7 repetitions as shown in Fig. 7b. It was obtained from this experiment that the calculated % RSD for HQ, DA, and UA were kept at 3.08, 1.08, and 0.99%, respectively. Thus, this work displayed an excellent stability of RGO/MWCNT (1 : 1)-modified GCE for simultaneous measurements of HQ, DA, and UA.

The investigation of selectivity studies was performed using the DPV technique by measuring a solution containing 50 μM UA, 30 μM DA, and 10 μM UA in 0.1 M of pH 7 phosphate buffer in the presence of several possible interfering species such as Mg^{2+}, K^{+}, Cl^{-}, ascorbic acid, and glucose. As shown in Fig. 7c, the current response of RGO/MWCNT (1 : 1)-modified GCE in the presence of several interfering species displays can be

maintained with a small influence indicated by its RSD value of 2.31%. Furthermore, this selectivity investigation also yielded a recovery value in the recovery range of 96–102% (Table 2) which can be assumed to be accepted in the analytical range.[103] In addition, the proposed sensor based on RGO/MWCNT (1 : 1)-modified GCE shows a negligible change in the current response for simultaneous measurement of HQ, DA, and UA during the initial seven days as depicted in Fig. 7d. The electrode based on RGO/MWCNT (1 : 1)-modified GCE can retain 80.5% of its original value of current intensity for these three analytes until seven days. Thus, the proposed sensor based on RGO/MWCNT (1 : 1)-modified GCE shows a good analytical performance for simultaneous detection of HQ, DA, and UA and potential for use in real samples such as from human urine.

3.7. Simultaneous determination of HQ, DA, and UA in the samples of human urine

To assess the performance of RGO/MWCNT (1 : 1)-modified GCE for simultaneous detection of HQ, DA, and UA for practical applications, this proposed sensor was applied in the samples of human urine taken from 6 volunteers. Informed consent was acquired for any experiments with human subjects. Before the measurements were conducted, 6 samples of human urines were diluted 100 times using 0.1 M of pH 7 phosphate buffer to

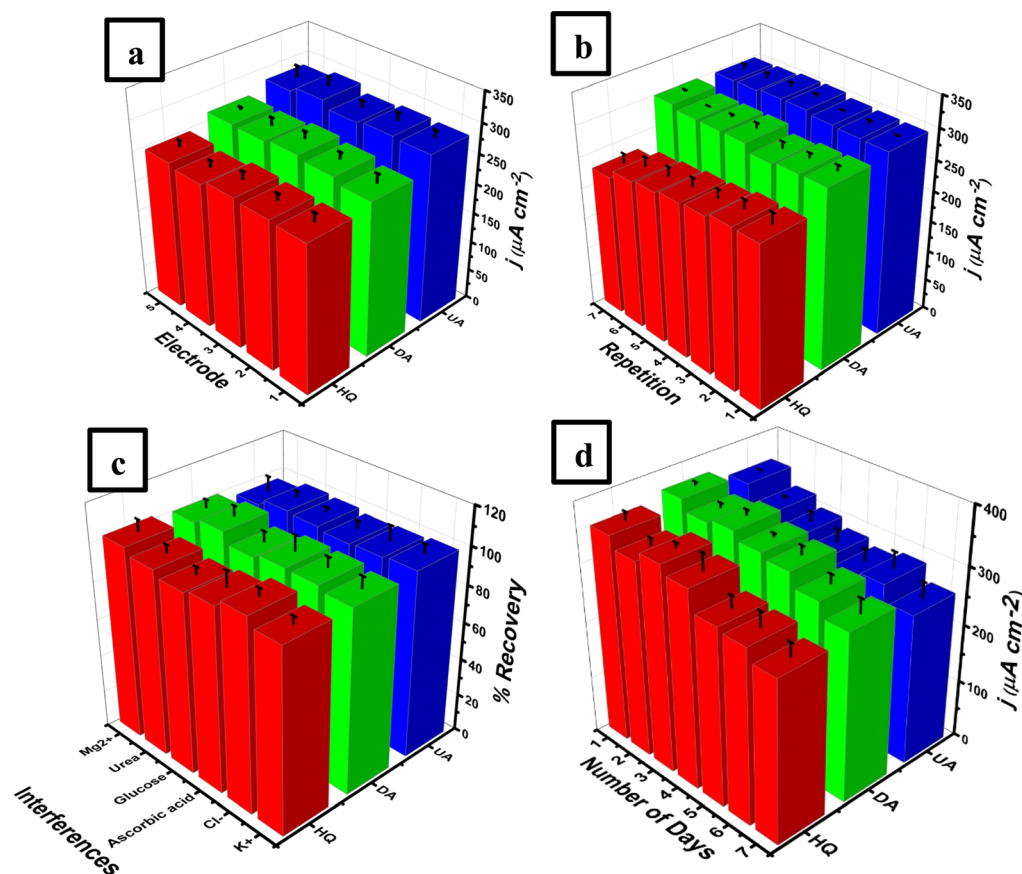Fig. 7   The current response of RGO/MWCNT (1 : 1)-modified GCE for the measurements of 50 μM UA, 30 μM DA, and 10 μM UA in 0.1 M of pH 7 phosphate buffer (a) using 5 different electrodes, (b) in 7 repetitions, and (c) in the presence of interference species (urea, glucose, ascorbic acid, Mg^{2+}, K^{+}, Cl^{-}). (d) The storage stability of RGO/MWCNT (1 : 1)-modified GCE in 7 days measurements.

Table 2 Effect of interfering species and its recovery value for the determination of 50 μM UA, 30 μM DA, and 10 μM UA in the 0.1 M of pH 7 phosphate buffer

Interferences	Interferences ratio level			Recovery (%)		
	(Interference : HQ)	(Interference : DA)	(Interference : UA)	HA	DA	UA
K^+	1 : 1	2 : 1	5 : 1	97.4	97.8	99.5
Cl^-	1 : 1	2 : 1	5 : 1	102.1	100.1	98.4
Ascorbic acid	1 : 1	2 : 1	5 : 1	98.1	100.4	97.6
Glucose	1 : 1	2 : 1	5 : 1	96.2	97.7	99.2
Urea	1 : 1	2 : 1	5 : 1	99.3	103.3	100.0
Mg^{2+}	1 : 1	2 : 1	5 : 1	102.6	100.7	96.4

Table 3 The average percentage of recoveries obtained from the simultaneous determination of HQ, DA, and UA in different human urine samples

Sample	Percentage of recovery (%)		
	HQ	DA	UA
Urine 1	98.8 ± 2.6	97.0 ± 2.3	98.0 ± 2.4
Urine 2	103.6 ± 1.5	97.8 ± 2.2	98.0 ± 3.5
Urine 3	103.4 ± 1.5	96.6 ± 0.9	99.2 ± 3.6
Urine 4	101.2 ± 2.5	99.8 ± 2.4	97.2 ± 1.6
Urine 5	101.0 ± 2.2	99.6 ± 1.5	97.4 ± 2.4
Urine 6	100.0 ± 2.3	97.8 ± 1.1	97.2 ± 2.4

avoid any interference from the real samples. Then the urine samples were spiked with different concentrations of HQ (5, 10, 15, 20, and 25 μM), DA (3, 6, 9, 12, and 15 μM), and UA (1, 2, 3, 4, and 5 μM). Based on Table 3, the average percentage recoveries obtained from 6 samples of human urines in triplicate measurements were discovered between 98–101% for HQ, 96–99% for DA, and 97–98% for UA. Data in detail was provided in Table S1 in the ESI section.† This result indicates that this proposed sensor could be developed further as a disposable electrode due to its simplicity of electrode modifier materials which can be applied to the planar substrate for rapid measurements of biomolecules in real samples.

4 Conclusions

In this work, we have successfully developed the electrochemical sensor based on the composite of RGO and MWCNT-modified GCE for the simultaneous detection of HQ, DA, and UA in synthetic standard solutions and real samples. It was revealed that the composition of RGO with MWCNT as 1 : 1 in each concentration of 1 mg mL^{-1} exhibits the highest electrocatalytic activity towards simultaneous measurements of HQ, DA, and UA compared to other weight ratios. This is due to the synergistic effect between RGO and MWCNT related to noncovalent interactions and van der Waals forces resulting in clear improvement in the signal discrimination and response capabilities in detecting HQ, DA, and UA simultaneously. These beneficial properties of the RGO/MWCNT composite contribute to the lower limit of detection of HQ, DA, and UA as 0.8, 1, and 0.6 μM, respectively. In addition, the proposed sensor also displays several benefits for simultaneous detection of HQ, DA, and UA including wide linear range, excellent sensitivity and selectivity, outstanding repeatability, and long-term stability. This proposed sensor also demonstrated an effective detection for simultaneous measurements of HQ, DA, and UA in 6 samples of human urine with a satisfactory result. Thus, the proposed sensor based on a composite of RGO and MWCNT has the potency to be developed for *in situ* monitoring with minimal costs which is important for point-of-care applications. Furthermore, this proposed method offers an alternative way for the simultaneous detection of biomolecule target species which in traditional procedures require expensive equipment and a complex sample pretreatment process. These features made this proposed sensor attractive to the application of routine analysis.

Data availability

The authors confirm that the data supporting the findings of this study are available within the article and/or its ESI.†

Informed consent

Informed consent was obtained from all volunteers who contributed human urine to this work.

Author contributions

The author's contributions to this article are as follows: writing, supervision, review, and funding acquisition: Wulan Tri Wahyuni. Data acquisition: Shafa Aini Hasnawati Ta'alia, Bunga Rani Elvira, Ari Yustisia Akbar. Conceptualization and funding: Irkham, Isnaini Rahmawati, Ruri Agung Wahyuono. Writing – original draft, supervision, review, conceptualization: Budi Riza Putra.

Conflicts of interest

There are no conflicts to declare.

Acknowledgements

References

1 R. Manikandan, T. Rajarathinam, S. Jayaraman, H.-G. Jang, J.-H. Yoon, J. Lee, H.-J. Paik and S.-C. Chang, *Coord. Chem. Rev.*, 2024, **499**, 215487, DOI: **10.1016/j.ccr.2023.215487**.

2 M.-B. Irimes, A. Pusta, A. Cernat, B. Feier, M. Tertis, C. Cristea, A. D. Buzoianu and R. Oprean, *TrAC, Trends Anal. Chem.*, 2024, **172**, 117560, DOI: **10.1016/j.trac.2024.117560**.

3 N. Li, J.-R. Huang, H.-Y. Zhang, M. Cui, B. Sun, C. Zhang and H.-Y. Zhao, *ACS Appl. Nano Mater.*, 2024, **7**, 1960–1969, DOI: **10.1021/acsanm.3c05232**.

4 Y. Niu, K. Kang, B. Wang, L. Wang, C. Li, X. Gao, Z. Zhao and X. Ji, *Talanta*, 2024, **268**, 125349, DOI: **10.1016/j.talanta.2023.125349**.

5 Y. Xing, C. Lv, Y. Fu, L. Luo, J. Liu, X. Xie and F. Chen, *Talanta*, 2024, **271**, 125674, DOI: **10.1016/j.talanta.2024.125674**.

6 T. S. I. Bakavaty and K. Gurunathan, *Mater. Sci. Eng., B*, 2024, **299**, 116967, DOI: **10.1016/j.mseb.2023.116967**.

7 A. Valenzuela, D. Ballestero, C. Gan, G. Lorca, E. Langa and M. R. Pino-Otin, *Toxics*, 2024, **12**, 115, DOI: **10.3390/toxics12020115**.

8 P. Prateek, P. Kumar, R. K. Gupta, V. C. Srivastava, I. D. Mall and U. L. Stangar, *J. Indian Chem. Soc.*, 2024, **101**, 101131, DOI: **10.1016/j.jics.2024.101131**.

9 M. M. Alam, M. Imran, T. Alshahrani, F. Khan and R. Azim, *Measurement*, 2024, **224**, 113890, DOI: **10.1016/j.measurement.2023.113890**.

10 X. Wang, H. Liu, Y. Xue, L. Cui, L. Chen, K.-F. Ho and Y. Huang, *Environ. Chem. Lett.*, 2024, **22**, 1327–1343, DOI: **10.1007/s10311-024-01701-x**.

11 O. D. Bamidele, B. A. Kayode, O. I. Eniayewu, A. J. Adegbola, R. S. Olatoye, N. S. Njinga, S. T. Abdullahi and M. T. Bakare-Odunola, *Sci. Rep.*, 2023, **13**, 20992, DOI: **10.1038/s41598-023-47160-2**.

12 J. J. Nordlund, P. E. Grimes and J. P. Ortonne, *J. Eur. Acad. Dermatol. Venereol.*, 2006, **20**, 781–787, DOI: **10.1111/j.1468-3083.2006.01670.x**.

13 A. P. DeCaprio, *Crit. Rev. Toxicol.*, 1999, **29**, 283–330, DOI: **10.1080/10408449991349221**.

14 F. Zhou, H. N. Lim, I. Ibrahim, N. A. Endot, E. A. Malek and N. S. K. Gowthaman, *ChemPlusChem*, 2024, **89**, e202300686, DOI: **10.1002/cplu.202300686**.

15 L. Lin, M. Li, P. Li, C. Ye, H. Zhuang, S. Weng and F. Chen, *Microchem. J.*, 2024, **196**, 109602, DOI: **10.1016/j.microc.2023.109602**.

16 C. V. Raju, R. Ramya, K. Imran, C. K. Basha, J. Wilson, T. Boobalan, A. Arun, M. J. Basu and S. Saravanan, *Microchem. J.*, 2024, **198**, 110189, DOI: **10.1016/j.microc.2024.110189**.

17 C. Liu, X. Lin, J. Liao, M. Yang, M. Jiang, Y. Huang, Z. Du, L. Chen, S. Fan and Q. Huang, *Chin. Chem. Lett.*, 2024, 109598, DOI: **10.1016/j.cclet.2024.109598**.

18 Y. Xue, Q. Hassan, M. Noroozifar, R. M. A. Sullan and K. Kerman, *Talanta*, 2024, **266**, 125030, DOI: **10.1016/j.talanta.2023.125030**.

19 F. Chen, J. Wang, L. Chen, H. Lin, D. Han, Y. Bao, W. Wang and L. Niu, *Anal. Chem.*, 2024, **96**, 3914–3924, DOI: **10.1021/acs.analchem.3c05672**.

20 G. Deffo, C. G. Fotsop, M. C. D. Ngaha, S. G. Fogang, L. A. Vomo, B. W. Nkuigoua, C. A. Shella, A. V. Somba, T. F. N. Tene, I. K. Tchummegne, E. Njanja, I. K. Tonle, P. Puzari and E. Ngameni, *Mater. Adv.*, 2024, **5**, 3683–3695, DOI: **10.1039/D3MA01182H**.

21 M. A. Khairy, A. Hamad, M. Hamed, M. Locatelli and F. T. Mansour, *J. Pharm. Biomed. Anal.*, 2024, **242**, 116021, DOI: **10.1016/j.jpba.2024.116021**.

22 J. S. Jeon, B. H. Kim, S. H. Lee, H. J. Kwon, H. J. Bae, S. K. Kim, J. A. Park, J. H. Shim, A. M. A. El-Aty and H. C. Shin, *Int. J. Cosmet. Sci.*, 2015, **37**, 567–573, DOI: **10.1111/ics.12228**.

23 B. P. Guiard and G. Gotti, *Molecule*, 2024, **29**, 496, DOI: **10.3390/molecules29020496**.

24 R. Cabrera-Alonso, E. Guevara, M. G. Ramirez-Elias, B. Moncada and F. J. Gonzalez, *Sking Res. Technol.*, 2018, **25**, 20–24, DOI: **10.1111/srt.12589**.

25 R. Cabrera-Alonso, E. Guevara, M. G. Ramirez-Elias, B. Moncada and F. J. Gonzalez, *J. Nanophotonics*, 2019, **13**(3), 036006, DOI: **10.1117/1.JNP.13.036006**.

26 I. B. Ansah, W.-C. Lee, C. W. Mun, J.-J. Rham, H. S. Jung, M. Kang, S.-G. Park and D.-H. Kim, *Sens. Actuators, B*, 2022, **353**, 131196, DOI: **10.1016/j.snb.2021.131196**.

27 A. Rybina, B. Thaler, R. Kramer and D.-P. Herten, *Phys. Chem. Chem. Phys.*, 2014, **16**, 19550–19555, DOI: **10.1039/C4CP02640C**.

28 H. Huang, J. Bai, L. Lei, W. Zhang, S. Yan and Y. Li, *Anal. Bioanal. Chem.*, 2020, **412**, 5291–5297, DOI: **10.1007/s00216-020-02742-1**.

29 Y.-H. Lin, Y.-H. Yang and S.-M. Yu, *J. Pharm. Biomed. Anal.*, 2007, **44**, 279–282, DOI: **10.1016/j.jpba.2007.02.004**.

30 X. Li, J. Pan, F. Yang, J. Feng, J. Mo and Z. Chen, *Microchim. Acta*, 2011, **174**, 123–130, DOI: **10.1007/s00604-011-0592-5**.

31 S. Zhao, J. Wang, F. Ye and Y.-M. Liu, *Anal. Biochem.*, 2008, **378**, 127–131, DOI: **10.1016/j.ab.2008.04.014**.

32 C. Shao-bo, P. Yun-yue, Y. Wen-Jing and X. Zhen-dong, *Anal. Test. Technol. Instrum.*, 2017, **23**, 176–179, DOI: **10.16495/j.1006-3757.2017.03.006**.

33 A. Chisvert, J. Sisternes, A. Balaguer and A. Salvador, *Talanta*, 2010, **81**, 530–536, DOI: **10.1016/j.talanta.2009.12.037**.

34 Q. Li, S. Wei, D. Wu, C. Wen and J. Zhou, *BioMed Res. Int.*, 2018, 3461572, DOI: **10.1155/2018/3461572**.

35 C. Xu, Q. Zheng, P. Zhao, J. Paterson, H. Chen and J. Am, *Soc. Mass Spectrochem.*, 2019, **30**, 685–693, DOI: **10.1007/s13361-018-2116-6**.

36 G. Mo, X. He, C. Zhou, D. Ya, J. Feng, C. Yu and B. Deng, *Sens. Actuators, B*, 2018, **266**, 784–792, DOI: **10.1016/j.snb.2018.03.187**.

37 Z. Dong, S. Xia, A. M. A. Alboull, I. M. Mostafa, A. Abdussalam, W. Zhang, S. Han and G. Xu, *ACS Appl.*

Nano Mater., 2024, **7**, 2983–2991, DOI: **10.1021/acsanm.3c05309**.

38 M. Kong, W. Wei, W. Wang, H. Chen and J. He, *Spectrochim. Acta, Part A*, 2021, **257**, 119773, DOI: **10.1016/j.saa.2021.119773**.

39 J. Qian, Z. Yang, H. Cui, K. An, C. Ren, Q. Liu and K. Wang, *J. Electroanal. Chem.*, 2020, **868**, 114177, DOI: **10.1016/j.jelechem.2020.114177**.

40 F. A. Gorla, M. d. P. Ferreira, C. S. d. Santos, R. d. Matos, M. G. Segatelli and C. R. T. Tarley, *J. Electroanal. Chem.*, 2024, **935**, 117988, DOI: **10.1016/j.jelechem.2023.117988**.

41 X. Ma, L. Deng, Z. Zou, Z. Pan, L. Feng, Z. Huang, Z. Liang, X. Liu, M. Li, Z. Su and H. Zheng, *Talanta*, 2024, **271**, 125646, DOI: **10.1016/j.talanta.2024.125646**.

42 M. P. Manikanta, R. R. Nikam, G. Tigari and N. B. Mallana, *Anal. Methods*, 2024, **16**, 1770–1784, DOI: **10.1039/D4AY00087K**.

43 S. P. Jyothi, D. Vinod, D. Chandran, S. Antherjanam, B. Saraswathyamma, V. Balaraman and R. Rajamani, *J. Appl. Electrochem.*, 2024, **54**, 1819–1831, DOI: **10.1007/s10800-024-02067-2**.

44 Z. Aryan, H. Khajehsharifi and S. Shahrokhian, *Microchem. J.*, 2024, **198**, 110087, DOI: **10.1016/j.microc.2024.110087**.

45 R. Wang, S. Liu, X. Song, K. Jiang, Y. Hou, Q. Cheng, W. Miao, L. Tian, Y. Ren and S. Xu, *Coatings*, 2024, **14**, 227, DOI: **10.3390/coatings14020227**.

46 J. Suriyaprakash, I. Thangavelu, Y. Huang, Z. Hu, H. Wang, Y. Zhan, L. Wu and L. Shan, *Surf. Interfaces*, 2024, **46**, 104021, DOI: **10.1016/j.surfin.2024.104021**.

47 V. Mariyappan, R. Sundaresan, S.-M. Chen, R. Ramachandran, A. G. Al-Sehemi, A. Jeevika and W. Wu, *Process Saf. Environ. Prot.*, 2024, **185**, 726–738, DOI: **10.1016/j.psep.2024.03.013**.

48 K. Prabhu, S. J. Malode, N. P. Shetti, S. Pandiaraj, A. Alodhayb and M. Muthuramamoorthy, *Microchem. J.*, 2024, **197**, 109722, DOI: **10.1016/j.microc.2023.109722**.

49 M. H. Rahman, M. A. Rashed, N. I. Nayem, M. A. Rahaman, J. Ahmed, M. Faisal, M. Jalalah and F. A. Harraz, *Mater. Chem. Phys.*, 2024, **314**, 128915, DOI: **10.1016/j.matchemphys.2024.128915**.

50 L. Zhang, H. Wu, Y. Chen, Y. Li, J. Xu, Y. Zhang, W. Wang, G. Zhao, C. Zhang and H. Li, *ACS Appl. Electron. Mater.*, 2024, **6**, 793–805, DOI: **10.1021/acsaelm.3c01322**.

51 H. Wang, Y. Hao, L. Xiang, X. Qi, L. Wang, J. Ding, Y. Qu, J. Xu and W. Zhing, *Mater. Res. Bull.*, 2024, **171**, 112631, DOI: **10.1016/j.materresbull.2023.112631**.

52 S.-H. Kim, T. H. Kim, H. K. Park, Y. C. Kang, J. S. Cho and G. D. Park, *J. Energy Storage*, 2024, **83**, 110683, DOI: **10.1016/j.est.2024.110683**.

53 H. Bagheri, A. Hajian, M. Rezaei and A. Shirzadmehr, *J. Hazard. Mater.*, 2017, **324**, 762–772, DOI: **10.1016/j.jhazmat.2016.11.055**.

54 Z.-N. Huang, J. Zou, J. Teng, Q. Liu, M.-M. Yuan, F.-P. Jiao, X.-Y. Jiang and J.-G. Yu, *Ecotoxicol. Environ. Saf.*, 2019, **172**, 167–175, DOI: **10.1016/j.ecoenv.2019.01.091**.

55 C. Ma, P. Xu, H. Chen, J. Cui, M. Guo and J. Zhao, *Microchem. J.*, 2022, **180**, 107533, DOI: **10.1016/j.microc.2022.107533**.

56 S. Yang, M. Yang, Q. Liu, X. Wang, H. Fa, Y. Wang and C. Hou, *J. Electrochem. Soc.*, 2019, **166**, B547, DOI: **10.1149/2.0011908jes**.

57 H. Mesker, F. Achi, A. Zouaoui, S. Ha, M. Peacock and H. Belkhalfa, *Anal. Lett.*, 2022, **55**, 1466–1481, DOI: **10.1080/00032719.2021.2008951**.

58 S. C. Silva, R. M. Cardoso, E. M. Richter, R. A. A. Munoz and E. Nossol, *Mater. Chem. Phys.*, 2020, **250**, 123011, DOI: **10.1016/j.matchemphys.2020.123011**.

59 P. Pasakon, J. P. Mensing, D. Phokaratkul, C. Karuwan, T. Lomas, A. Wisitsorat and A. Tuantranont, *J. Appl. Electrochem.*, 2019, **49**, 217–227, DOI: **10.1007/s10800-018-1268-1**.

60 J.-S. Chen, Y. Li, M.-J. Yu and H.-L. Lee, *J. Environ. Anal. Chem.*, 2020, **100**, 774–788, DOI: **10.1080/03067319.2019.1640874**.

61 X. Qiu, L. Lu, J. Leng, Y. Yu, W. Wang, M. Jiang and L. Bai, *Food Chem.*, 2016, **190**, 889–895, DOI: **10.1016/j.foodchem.2015.06.045**.

62 B. R. Putra, U. Nisa, R. Heryanto, E. Rohaeti, M. Khalil, A. Izzataddini and W. T. Wahyuni, *Anal. Sci.*, 2022, **38**, 157–166, DOI: **10.2116/analsci.21P214**.

63 S. Li, S. Ali, Z. Zuhra, H. Shen, J. Qiu, Y. Zeng, K. Zeng, X. Wang, G. Xie and S. Ding, *Molecules*, 2023, **29**, 65, DOI: **10.3390/molecules29010065**.

64 K. Hiratochi, D. Terada, H. Suga, M. Okada, K. Bandon, T. Kodaira, T. Yamada, T. Shimizu, K. Saiki and T. Kubo, *Mater. Chem. Front.*, 2024, **8**, 814–823, DOI: **10.1039/D3QM00992K**.

65 H. Wang, A. Wang, H. Yin, Y. Ding and C. Li, *Mater. Sci. Eng.*, 2024, **300**, 117061, DOI: **10.1016/j.mseb.2023.117061**.

66 D. Lopez-Diaz, M. L. Holgado, J. L. Garcia-Fiero and M. M. Velazquez, *J. Phys. Chem. C*, 2017, **121**, 20489–20497, DOI: **10.1021/acs.jpcc.7b06236**.

67 A. Romero, M. P. Lavin-Lopez, L. Sanchez-Silva, J. L. Valverde and A. Paton-Carrero, *Mater. Chem. Phys.*, 2018, **203**, 284–292, DOI: **10.1016/j.matchemphys.2017.10.013**.

68 M. Sieradzka, C. Slusarczyk, R. Fryczkowski and J. Janicki, *J. Mater. Res. Technol.*, 2020, **9**, 7059–7067, DOI: **10.1016/j.jmrt.2020.05.026**.

69 L. Wang, Z. Lou, J. Deng, R. Zhang and T. Zhang, *ACS Appl. Mater. Interfaces*, 2015, **7**, 13098–13104, DOI: **10.1021/acsami.5b03978**.

70 P. Das, K. Ibrahim, K. Chakraborty, S. Ghosh and T. Pal, *Sci. Rep.*, 2024, **14**, 296, DOI: **10.1038/s41598-023-51040-0**.

71 N. Sebastian, W.-C. Yu, D. Balram, A. Patel, D. Kumar and V. K. Yadav, *Sens. Int.*, 2024, **5**, 100256, DOI: **10.1016/j.sintl.2023.100256**.

72 B. Liang, H. Hu, H. Zhu, Y. Yu, W. He and G. Li, *Sci. Total Environ.*, 2024, **908**, 168466, DOI: **10.1016/j.scitotenv.2023.168466**.

73 M. Arslanhan and E. D. S. Parmak, *Thin Solid Films*, 2024, **788**, 140149, DOI: **10.1016/j.tsf.2023.140149**.

74 P. A Koyale, S. P. Kulkarni, J. L. Gunjakar, T. D. Dongale, S. S. Sutar, S. S. Soni, Y. G. Kapdi, R. Nath, S. V. Mulik and S. D. Delekar, *ACS Appl. Nano Mater.*, 2024, **7**, 2662–2674, DOI: **10.1021/acsanm.3c04694**.

75 F. Y. Ban, S. Jayabal, A. Pandikumar, H. N. Lim and N. M. Huang, *Electrocatalysis*, 2015, **6**, 373–381, DOI: **10.1007/s12678-015-0254-1**.

76 A. Benchirouf, C. Muller and O. Kanoun, *Nanoscale Res. Lett.*, 2016, **11**, 4, DOI: **10.1186/s11671-015-1216-5**.

77 Q. Kong, Z. Luo, Y. Wang and B. Wang, *J. Polym. Res.*, 2018, **25**, 231, DOI: **10.1007/s10965-018-1597-0**.

78 Q. Liu, J. Bao, M. Yang, X. Wang, S. Lan, C. Hou, Y. Wang and H. Fa, *Sens. Actuators, B*, 2018, **274**, 433–440, DOI: **10.1016/j.snb.2018.07.146**.

79 B. Liu, H. Guo, L. Sun, Z. Pan, L. Peng, M. Wang, N. Wu, Y. Chen, X. Wei and W. Yang, *Colloids Surf., A*, 2022, **639**, 128335, DOI: **10.1016/j.colsurfa.2022.128335**.

80 A. C. Anithaa, N. Lavanya, K. Asokan and C. Sekar, *Electrochim. Acta*, 2015, **167**, 294–302, DOI: **10.1016/j.electacta.2015.03.160**.

81 S. A. Shahamirifard, M. Ghaedi, Z. Razmi and S. Hajati, *Biosens. Bioelectron.*, 2018, **114**, 30–36, DOI: **10.1016/j.bios.2018.05.009**.

82 X. Yang, C. He, W. Lin, Y. Qiu, P. Li, Y. Chen, B. Huang and X. Zheng, *Synth. Met.*, 2022, **287**, 117079, DOI: **10.1016/j.synthmet.2022.117079**.

83 U. Amara, M. T. Mehran, B. Sarfaraz, K. Mahmood, A. Hayat, M. Nasir, S. Riaz and M. H. Nawaz, *Microchim. Acta*, 2021, **188**, 230, DOI: **10.1007/s00604-021-04884-0**.

84 N. Vishnu, M. Gandhi, D. Rajagopal and A. S. Kumar, *Anal. Methods*, 2017, **9**, 2265–2274, DOI: **10.1039/C7AY00445A**.

85 P. Karami-Kolmoti, H. Beitollahi and S. Modiri, *Biomedicines*, 2023, **11**, 1869, DOI: **10.3390/biomedicines11071869**.

86 C. W. Atcherley, N. D. Laude, E. B. Monroe, K. M. Wood, P. Hashemi and M. L. Heien, *ACS Chem. Neurosci.*, 2015, **6**, 1509–1516, DOI: **10.1021/cn500020s**.

87 S. A. Shahamirifard, M. Ghaedi, Z. Razmi and S. Hajati, *Biosens. Bioelectron.*, 2018, **114**, 30–36, DOI: **10.1016/j.bios.2018.05.009**.

88 S. Kostromin, M. Asandulesa, A. Poldshivalov and S. Bronnikov, *Mater. Res. Express*, 2019, **6**, 115053, DOI: **10.1088/2053-1591/ab46f8**.

89 K. A. Shiyanova, M. V. Gudkov, M. K. Torkunov, G. P. Goncharuk, A. A. Gulin, A. V. Sysa, N. G. Ryvkina, S. L. Bazhenov and V. P. Melnikov, *J. Compos. Mater.*, 2023, **57**, 111–119, DOI: **10.1177/0021998322113954**.

90 S. Liang, H. Wang and X. Tao, *J. Mater. Res. Technol.*, 2022, **17**, 2388–2399, DOI: **10.1016/j.jmrt.2022.02.004**.

91 O. Okhay and A. Tkach, *Nanomaterials*, 2021, **11**, 1240, DOI: **10.3390/nano11051240**.

92 N. S. Suhaimin, M. F. R. Hanifah, M. Azhar, J. Jaafar, M. Aziz, A. F. Ismail, M. H. D. Othman, M. A. Rahman, F. Aziz, N. Yusof and R. Mohamud, *Mater. Chem. Phys.*, 2022, **278**, 125629, DOI: **10.1016/j.matchemphys.2021.125629**.

93 T. Thenrajan, M. M. Malar, S. Kumaravel, R. Rajaram, S. Kundu and J. Wilson, *Mater. Adv.*, 2024, **5**, 1691–1701, DOI: **10.1039/D3MA00533J**.

94 V. Stankovic, S. Durdic, M. Ognjanovic, G. Zlatic and D. Stankovic, *Sensors*, 2024, **24**, 705, DOI: **10.3390/s24020705**.

95 Y. Zhang, X. Du, J. Mao, S. He and Z. Cao, *Mater. Chem. Phys.*, 2024, **311**, 128526, DOI: **10.1016/j.matchemphys.2023.128526**.

96 J. Li, L. Hou, Y. Jiang, M.-J. Wei, F.-Y. Kong, H.-Y. Li, Z.-X. Wang and W. Wang, *Microchem. J.*, 2024, **199**, 110007, DOI: **10.1016/j.microc.2024.110007**.

97 Y. Liao, L. Lin, J. Liu, X. Zhang and X. Li, *J. Electroanal. Chem.*, 2024, **954**, 118028, DOI: **10.1016/j.jelechem.2024.118028**.

98 Y.-Y. Lei, X. Zhan, Y.-W. Wu and X.-X. Yu, *Talanta*, 2024, **268**, 125287, DOI: **10.1016/j.talanta.2023.125287**.

99 Z. Feng, H. N. Lim, I. Ibrahim, N. A. Endot, E. A. Malek and N. S. K. Gowthaman, *Appl. Organomet. Chem.*, 2024, **38**, e7350, DOI: **10.1002/aoc.7350**.

100 E. D. Tecuapa-Flores, C. B. Palacios-Cabrera, A. J. Santiago-Cuevas, J. G. Hernandez, J. Narayanan and P. Thangarasu, *Analyst*, 2024, **149**, 108–124, DOI: **10.1039/D3AN01467C**.

101 D. Jia, T. Yang, K. Wang, L. Zhou, E. Wang, K.-C. Chou, H. Wang and X. Hou, *J. Alloys Compd.*, 2024, **985**, 173392, DOI: **10.1016/j.jallcom.2023.173392**.

102 S. A. H. Ta'alia, E. Rohaeti, B. R. Putra and W. T. Wahyuni, *Results Chem.*, 2023, **6**, 101024, DOI: **10.1016/j.rechem.2023.101024**.

103 S. Lu, K. Zhang, Y. Liu, X. Zhan and R. Savari, *Environ. Res.*, 2024, **245**, 117369, DOI: **10.1016/j.envres.2023.117369**.